

The Star-Forming Molecular Gas in High Redshift Submillimeter Galaxies

Desika Narayanan^{*†}, Thomas J. Cox[‡], Christopher C. Hayward, Joshua D. Younger, and Lars Hernquist

Harvard-Smithsonian Center for Astrophysics, 60 Garden St., Cambridge, Ma 02138

Submitted to MNRAS

ABSTRACT

We present a model for the CO molecular line emission from high redshift Submillimeter Galaxies (SMGs). By combining hydrodynamic simulations of gas rich galaxy mergers with the polychromatic radiative transfer code, SUNRISE, and the 3D non-LTE molecular line radiative transfer code, TURTLEBEACH, we show that if SMGs are typically a transient phase of major mergers, their observed compact CO spatial extents, broad line widths, and high excitation conditions (CO SED) are naturally explained. In this sense, SMGs can be understood as scaled-up analogs to local ULIRGs. We utilize these models to investigate the usage of CO as an indicator of physical conditions. We find that care must be taken when applying standard techniques. The usage of CO line widths as a dynamical mass estimator from SMGs can possibly overestimate the true enclosed mass by a factor ~ 1.5 -2. At the same time, assumptions of line ratios of unity from CO J=3-2 (and higher lying lines) to CO (J=1-0) will oftentimes lead to underestimates of the inferred gas mass. We provide tests for these models by outlining predictions for experiments which are imminently feasible with the current generation of bolometer arrays and radio-wave spectrometers.

Key words: cosmology:theory–galaxies:formation–galaxies:high-redshift–galaxies:starburst–galaxies:ISM–galaxies:ISM–ISM:molecules

1 INTRODUCTION

Understanding the origin and evolution of active galaxy populations at cosmological redshifts remains an outstanding problem. Of particular interest are a population of submillimeter-luminous galaxies discovered via deep, blind surveys with SCUBA on the JCMT at a median redshift of $z \sim 2$ (Barger et al. 1998; Hughes et al. 1998; Chapman et al. 2003a). These Submillimeter Galaxies (SMGs) are empirically defined with the flux limit $S_{850\mu m} \gtrsim 5$ -6 mJy¹ (e.g. Blain et al. 2002), and appear to be a highly clustered population of galaxies forming stars at prodigious rates (SFR $\gtrsim 10^3 M_{\odot} \text{yr}^{-1}$; Blain et al. 2002, 2004; Swinbank et al. 2004; Menéndez-Delmestre et al. 2007; Kovács et al. 2006; Valiante et al. 2007; Coppin et al. 2008a). In addition to undergoing prodigious star formation, some SMGs additionally host heavily obscured AGN (e.g. Ivison et al. 2002; Alexander et al. 2005a,b, 2008; Borys et al. 2005). These galaxies may contribute a substantial fraction of the cosmic star formation

density (Blain et al. 1999, 2002), as well as serve as prime candidates for studying the coevolution of black hole growth and star formation at an epoch of heightened galaxy formation and evolution.

Many open questions remain regarding the physical nature of SMGs. Are they isolated galaxies, or galaxy mergers? What is their potential place in an evolutionary sequence? Are they high-redshift analogs to local infrared luminous galaxies (e.g. ULIRGs)? What are their typical gaseous and stellar masses?

Emission from the star forming molecular interstellar medium (ISM) has the potential to elucidate some of these questions. For example, ¹²CO (J=1-0; hereafter, CO) emission can serve as a measure both for the total amount of H₂ molecular gas available for future star formation (e.g. Downes & Solomon 1998; Solomon & Barrett 1991; Greve et al. 2005), as well as previous stellar mass assembly by serving as a dynamical mass tracer (e.g. Tacconi et al. 2006; Bouché et al. 2007; Ho 2007; Narayanan et al. 2008b). The high resolution images available from millimeter-wave interferometry can reveal source sizes and morphologies (e.g. Genzel et al. 2003; Tacconi et al. 2006, 2008; Younger et al. 2008; Iono et al. 2009). Additionally, the rotational ladder from H₂ tracers such as CO reveal the thermal conditions and mean densities of the star forming ISM (Weiß et al. 2005, 2007). CO has

* E-mail: dnarayanan@cfa.harvard.edu

† CfA Fellow

‡ W.M. Keck Postdoctoral Fellow

¹ This empirical definition is for blank-field surveys at current sensitivity limits.

been detected routinely in high redshift SMGs for over a decade (e.g. Frayer et al. 1998, 1999; Neri et al. 2003; Genzel et al. 2003; Greve et al. 2005; Tacconi et al. 2006, 2008, and references therein). During this time, a number of pioneering papers have afforded the community a wealth of CO data from $z \sim 2$ SMGs. The general molecular emission properties from SMGs can be summarized as follows.

H₂ Gas Masses: SMGs are incredibly gas rich, with massive H₂ gas reservoirs. Extrapolation from typical CO (J=3-2) rest frame measurements from SMGs suggests H₂ masses of order 10^{10} - 10^{11} M_⊙, making these some of the most molecular gas rich galaxies in the Universe (Greve et al. 2005; Solomon & Vanden Bout 2005; Tacconi et al. 2006; Carilli & Wang 2006; Tacconi et al. 2008; Coppin et al. 2008b). An analysis of semi-analytic models of SMG formation by Swinbank et al. (2008) found good agreement between the cold gas mass in their simulations and the observed values.

Line Widths: The CO line widths in SMGs are typically broad with median line width ranging from ~ 600 - 800 km s⁻¹ (FWHM; Greve et al. 2005; Carilli & Wang 2006; Tacconi et al. 2006; Coppin et al. 2008b; Tacconi et al. 2008; Iono et al. 2009). Comparisons to CO-detected quasars at comparable redshifts have had conflicting results. Analysis of literature data by Carilli & Wang (2006) has suggested that SMGs typically have broader line widths than $z \sim 2$ quasars by a factor of ~ 2.5 with KS tests indicating the two are not drawn from the same parent population at the $>99\%$ confidence level. On the other hand, new detections by Coppin et al. (2008b) have found rather similar CO line widths from quasars and SMGs, and KS tests showing that the two arise from the same parent population at the $>95\%$ confidence level.

Images: Interferometric CO imaging of SMGs has shown the spatial distribution of most SMGs to be relatively compact ($R_{\text{hwhm}} \lesssim 1$ - 2 kpc; Tacconi et al. 2006). Some individual sources have shown rather extended emission (e.g. Genzel et al. 2003). Curiously, images have shown evidence for compact disk-like motion in at least a few sources (Genzel et al. 2003; Tacconi et al. 2006), as well as extended emission in what appears to be interacting/merging galaxies (e.g. Ivison et al. 2001; Tacconi et al. 2006).

Excitation Properties: While very few SMGs have been observed in multiple CO lines, the existing data suggests that these galaxies exhibit relatively high molecular excitation conditions. The CO line spectral energy distributions (CO SEDs; alternatively known as CO rotational ladders) are seen to typically turn over at the J=5 level (~ 83 K above ground; Weiß et al. 2005, 2007; Greve et al. 2005; Hainline et al. 2006). That said, few objects have been detected in their rest-frame CO (J=1-0) line (Hainline et al. 2006). As H₂ masses are typically inferred from CO (J=1-0) measurements, the excitation properties of higher lying levels (e.g. line ratios) with respect to the ground state transition are crucial to constrain for the purposes of deriving molecular gas masses.

While the information provided by CO observations of $z \sim 2$ SMGs is indeed invaluable, questions remain regarding the interpretation of many of the various aforementioned observational characteristics of these sources. For example, what is the true relationship between CO line widths from SMGs and quasars? Is there an evolution in the CO line widths of SMGs? How reliably can the CO line width be used as dynamical mass tracer in these galaxies? How can observations of higher lying CO lines (in the rest frame) be extrapolated to the rest frame CO (J=1-0) luminosity in order to derive an H₂ gas mass (e.g. Hainline et al. 2006)? Can the observed CO emission line widths, excitation properties, and images be explained by a merger-driven scenario for SMG formation and

evolution (e.g. “scaled up ULIRGs”; Tacconi et al. 2006, 2008)? It is clear that a theoretical interpretation behind the molecular line emission properties may be valuable for elucidating some of the aforementioned issues, as well as providing interpretation for forthcoming observations.

Along with providing interpretation for observations, theoretical calculations of CO emission from simulated SMGs can provide direct tests of models of SMG formation and evolution. In Narayanan et al. (2009), we presented a merger-driven model for the formation of SMGs which reproduced the full range of observed 850 μm fluxes from SMGs, the optical-mm wave SED, and characteristic stellar, black hole, and dark matter masses. Comparing the simulated molecular gas properties of these model SMGs to the extensive data sets in the literature provides a strict test of the models. In this paper, we investigate the CO emission properties from SMGs by combining these SMG formation models with 3D non-local thermodynamic equilibrium (LTE) molecular line radiative transfer calculations (Narayanan et al. 2006a, 2008a). The goals of this paper are to: (a) provide direct tests of merger-driven formation mechanisms for SMGs by comparing the simulated CO emission from the models of Narayanan et al. (2009) to observations, and, given a sufficient correspondence between models and observations, (b) provide interpretation for existing and future observational data.

This paper is organized as follows: in § 2, we describe our numerical methods for our hydrodynamic, molecular line radiative transfer, and polychromatic SED radiative transfer simulations. In § 3, we summarize the evolution of the submillimeter, *B*-band, and H₂ properties of our simulated galaxies. In § 4.1, we study the CO morphology, molecular disk formation and CO spatial extents in SMGs. In § 4.2, we explore the origin of the broad observed CO line widths. We use these results to investigate the usage of CO as a dynamical mass tracer in § 5, and analyze the CO excitation in SMGs in § 6. In § 7, we provide imminently testable observational predictions, and in § 8, we summarize.

2 NUMERICAL METHODS

Generically, our methodology involves three steps. First, we simulate the hydrodynamic evolution of galaxies utilizing the smoothed-particle hydrodynamics (SPH) code, GADGET-3 (Springel 2005). We then calculate the molecular line emission properties and SEDs from these simulated galaxies in post-processing utilizing the radiative transfer codes TURTLEBEACH (Narayanan et al. 2008a) and SUNRISE (Jonsson et al. 2009). This method is summarized in the flowchart presented in Figure 1. In this section, we present the details of the hydrodynamic and radiative transfer methods.

2.1 Hydrodynamics

A major goal of our program is to understand the evolution of model SMGs while remaining constrained to observations for physical input to the simulations. When data for SMGs is unavailable, we turn to observational constraints from the Galaxy or local starbursts. We consider the formation of SMGs in gas rich binary galaxy mergers at high redshift. This is motivated by observed radio, CO, and optical morphologies of SMGs which appear to show signs of interactions (e.g. Chapman et al. 2003b; Tacconi et al. 2006, 2008), as well as theoretical models which demonstrate that mergers serve as an efficient means of triggering nuclear starbursts (Barnes & Hernquist 1991, 1996; Mihos & Hernquist 1994, 1996;

Table 1. SMGs are ordered with decreasing halo mass. Column 1 is the name of the model used in this work. Columns 2 & 3 are initial orientations for disk 1, Columns 4 & 5 are for disk 2. Column 6 gives the virial velocity of the progenitors, Column 7 gives their halo masses, and Column 8 the mass ratio of the merger. Please see Narayanan et al. (2009) for generalized results regarding the physical properties of these galaxies.

Model	θ_1	ϕ_1	θ_2	ϕ_2	V_c (km s^{-1})	M_{DM} M_\odot	Mass Ratio
SMG1	30	60	-30	45	500:500	2.5×10^{13}	1:1
SMG2	360	60	150	0	500:500	2.5×10^{13}	1:1
SMG3	-109	-30	71	-30	500:500	2.5×10^{13}	1:1
SMG4	30	60	-30	45	500:320	1.6×10^{13}	1:3
SMG5	360	60	150	0	500:320	1.6×10^{13}	1:3
SMG6	-109	-30	71	-30	500:320	1.6×10^{13}	1:3
SMG7	30	60	-30	45	500:225	1.4×10^{13}	1:12
SMG8	360	60	150	0	500:225	1.4×10^{13}	1:12
SMG9	-109	-30	71	-30	500:225	1.4×10^{13}	1:12
SMG10	30	60	-30	45	320:320	6.6×10^{12}	1:1
SMG11	360	60	150	0	320:320	6.6×10^{12}	1:1
SMG12	-109	-30	71	-30	320:320	6.6×10^{12}	1:1
SMG13	30	60	-30	45	225:225	2.35×10^{12}	1:1

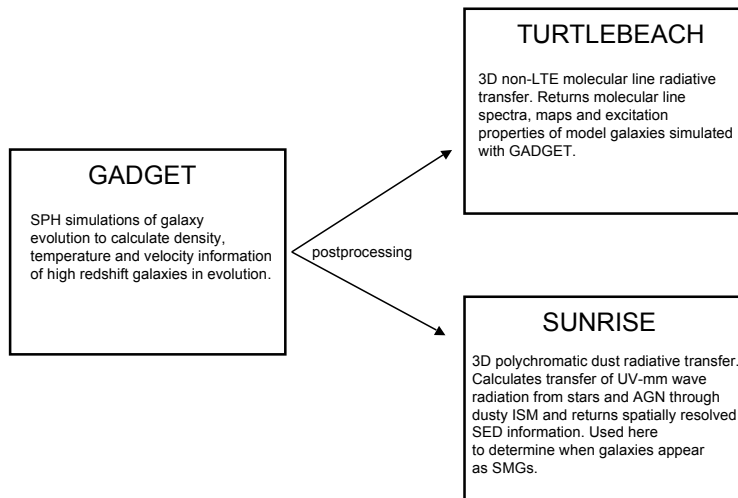


Figure 1. Flowchart summarizing methodology. The galaxies are simulated hydrodynamically using the SPH code, GADGET-3 (Springel 2005). The simulated molecular line emission and SEDs are then calculated in post-processing utilizing the radiative transfer codes TURTLEBEACH (Narayanan et al. 2008a) and SUNRISE (Jonsson et al. 2009), respectively.

Springel et al. 2005). Moreover, simulations by Narayanan et al. (2009) have suggested that isolated galaxies and minor mergers (mass ratio $\ll 1:10$) are unlikely to result in a $S_{850} > 5$ mJy SMG.

The hydrodynamic simulations were performed with the smoothed-particle hydrodynamics code, GADGET-3² (Springel 2005) which utilizes a fully conservative SPH formalism (Springel & Hernquist 2002). The hydrodynamic simulations include prescriptions for radiative cooling of the gas (Katz et al. 1996; Davé et al. 1999), and a multiphase ISM in which cold

clouds are considered to be in pressure equilibrium with hot gas (McKee & Ostriker 1977; Springel & Hernquist 2003). This multiphase ISM is implemented such that cold clouds grow through radiative cooling of hot gas, and heating from star formation can evaporate cold clouds (Springel et al. 2005). The effect of supernovae on the ISM is treated via an effective equation of state (EOS). Here, we employ the full multi-phase EOS where supernovae-driven pressure optimally maintain disk-stability ($q_{\text{EOS}}=1$; For more details, see Figure 4 of Springel et al. 2005).

Star formation occurs following a volumetric generalization of the Kennicutt-Schmidt relation, $\text{SFR} \propto n^{1.5}$ (Kennicutt 1998a,b; Kennicutt et al. 2007; Schmidt 1959; Springel & Hernquist 2003), which results in disks consistent with the local surface-density scaling relations (Cox et al. 2006). The star formation timescale is chosen such that isolated disk models are consistent with the normalization of the local Kennicutt-Schmidt relations. While there are rather few measurements of observed star formation rate (SFR) relations at cosmological redshifts, tentative evidence exists that $z \sim 2$ galaxies may lie on the present-day Kennicutt-Schmidt relation (Bouché et al. 2007). Indeed, this is theoretically favorable as the relation $\text{SFR} \sim n^{1.5}$ may be understood in terms of free-fall time arguments which are redshift invariant.

Black holes are included in the simulations as sink particles which accrete following a Bondi-Hoyle-Lyttleton parameterization according to the local gas density and sound speed (Bondi & Hoyle 1944; Bondi 1952). The bolometric luminosity of the black hole is set at $L_{\text{bol}} = \epsilon \dot{M} c^2$, where $\epsilon=0.1$. Feedback from the black hole(s) is modeled such that a fixed fraction of this luminosity (here, 5%) couples thermally and isotropically to the surrounding ISM. This coupling efficiency is set to match the normalization of the local $M - \sigma$ relation (Di Matteo et al. 2005; Springel et al. 2005).

The progenitor disk galaxies are initialized with a Hernquist (1990) dark matter halo profile (for details, see Springel et al. 2005) with virial properties scaled to be appropriate for $z \sim 3$ (such that they may represent galaxies undergoing a major merger by $z \sim 2$; Bullock et al. 2001; Robertson et al. 2006). The progenitors begin with an initial gas fraction of $f_g=0.8$, resulting in a gas fraction of $f_g \sim 20\text{-}40\%$ by the time the galaxies approach final coalescence. This is comparable to recent measurements by Bouché et al.

² The main improvement in GADGET-3 over GADGET-2 (described by Springel 2005) is better load balancing on parallel processors.

(2007) and Tacconi et al. (2008) who find tentative evidence for gas fractions in $z \sim 2$ SMGs of $\sim 40\%$.

Here, we consider the Narayanan et al. (2009) series of 12 models, varying total mass, mass ratio, and orbit. We include one additional lower mass merger which will not make an SMG (model SMG13), though will be useful for predictions of lower flux galaxies (§ 7). The initial conditions of the merger simulations are summarized in Table 2.1. The primary progenitors are initialized with circular velocities ranging from $V_c=320\text{--}500 \text{ km s}^{-1}$, similar to measurements tabulated by Tacconi et al. (2008). This corresponds to halo masses of order $M_{\text{DM}} \sim 10^{12}\text{--}10^{13} M_{\odot}$, comparable to those inferred by clustering measurements (Blain et al. 2004; Swinbank et al. 2008). We model the formation of SMGs in 1:1 mergers in $\sim 10^{12}$, 5×10^{12} , and $\sim 10^{13} M_{\odot}$ halos, and 1:3 and 1:12 mergers with a $M_{\text{DM}} \approx 10^{13} M_{\odot}$ primary galaxy. We utilize 3 different initial orbits for the galaxies. For clarity, throughout this work, we primarily focus on the results from a fiducial merger (in Table 2.1, model SMG10) which produces a relatively average $S_{850} \approx 5\text{--}7 \text{ mJy SMG}^3$. The CO results (next section) are generic for all models considered here. There is a dispersion amongst the simulated submillimeter fluxes when varying merger orbit (even at a constant galaxy mass; see Figure 2 of Narayanan et al. (2009) for a direct quantification of this dispersion). The fiducial SMGs studied here lie in the middle of this dispersion for given halo masses, and, as such, are typical. See Narayanan et al. (2009) for results regarding the physical properties of these merger simulations.

2.2 Radiative Transfer

2.2.1 Molecular Line Radiative Transfer

We utilize the 3D non-LTE molecular line radiative transfer code, TURTLEBEACH, to calculate the CO emission properties from our model SMGs (Narayanan et al. 2008a). TURTLEBEACH is an exact line transfer code that assumes full statistical equilibrium. The details of the code can be found in Narayanan et al. (2006b) and Narayanan et al. (2008a), and we refer the reader to these papers for details on the specific algorithms used. Here, we summarize the details relevant to this work.

We assume that all cold, star-forming gas in the hydrodynamic simulations is neutral. Following the observational constraints of Blitz & Rosolowsky (2006), we model the molecular fraction based on the ambient hydrostatic pressure:

$$R_{\text{mol}} = n_{\text{H}_2}/n_{\text{HI}} = \left[\frac{P_{\text{ext}}/k}{3.5 \times 10^4} \right]^{0.92} \quad (1)$$

where k is Boltzmann’s constant, and the external pressure P_{ext} is calculated via the fitting formula derived by Robertson et al. (2004):

$$\log P = 0.05(\log n_{\text{H}})^3 - 0.246(\log n_{\text{H}})^2 + 1.749(\log n_{\text{H}}) - 10.6(2)$$

³ When considering emission properties which are strongly dependent on merger mass, we will, at times, employ the usage of SMG1 as a “high-mass” fiducial SMG along with SMG10. This allows us to bracket the range of galaxy masses which form SMGs in our simulations. SMG1 forms an SMG ranging from average ($S_{850} \approx 5\text{--}7 \text{ mJy}$ during inspiral) to extremely luminous and rare ($S_{850} \approx 15 \text{ mJy}$ during final coalescence), whereas SMG10 forms at peak (final coalescence) only an average $S_{850} \approx 5\text{--}7 \text{ mJy}$ SMG. See Narayanan et al. (2009) for more details regarding the lightcurve of model SMG1.

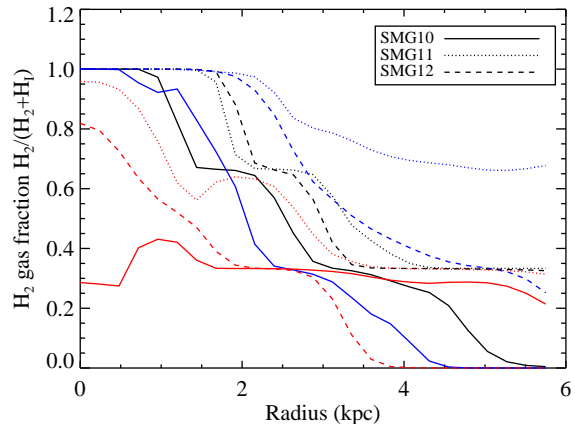


Figure 2. Radially averaged molecular gas fraction as a function of galactocentric radius for three model SMGs (varying only the orientation angle of the disks) during three different phases. The three model SMGs produce “average” SMGs with fluxes ranging from $S_{850} \approx 2\text{--}7 \text{ mJy}$ (Narayanan et al. 2009). The black lines are the pre-merger phase for each model; the blue lines denote the peak of the starburst (roughly the peak of the SMG phase); and the red lines represent the post-quasar phase. The molecular gas fraction is calculated via a dependency on the ambient pressure as motivated by observations of clouds in local galaxies (Blitz & Rosolowsky 2006). During the peak of the SMG phase (blue lines), the bulk of the neutral gas in the central regions is molecular, owing to rather high gas densities in the galactic nucleus.

In Figure 2, we show the radially averaged molecular gas fraction as a function of galactocentric distance for three model SMGs⁴.

In order to investigate numerous snapshots at relatively high temporal resolution (5 Myr) for a number of merger models, the hydrodynamic simulations were smoothed to a spatial resolution of $\sim 160 \text{ pc}$. Resolution tests presented in Narayanan et al. (2008a) which investigated the spectral and spatial invariance of these methods confirm that the resultant CO morphologies, lines profiles, and excitation conditions are convergent at these spatial resolutions. In order to properly account for the molecular density gradients which exist within cells of this volume (i.e. dense cloud cores and diffuse cloud atmospheres), we further model the molecular gas following the sub-grid prescriptions of Narayanan et al. (2008a). Specifically, the molecular gas within the $\sim 160 \text{ pc}$ grid cells is assumed to reside in a mass spectrum of GMCs which are modeled as singular isothermal spheres. The mass spectrum of clouds follows a power-

⁴ We note that this feature of the code is an improvement over the algorithms described in Narayanan et al. (2008a). Specifically, previous works using TURTLEBEACH have assumed half the neutral gas (by mass) was molecular, consistent with average conditions in local galaxies (Keres et al. 2003). While these assumptions tying the molecular gas fraction to global observations may reproduce average molecular emission patterns in galaxies and AGN (e.g. Narayanan et al. 2006a, 2008b,a,c), it does not provide spatially resolved information regarding the molecular content. By tying the molecular gas fraction to the ambient pressure as motivated by observations of GMCs (Blitz & Rosolowsky 2006), we are able to more accurately model the spatial distribution of the molecular gas. We note that even more sophisticated models for treating the neutral gas breakdown exist in the literature (e.g. Pelupessy et al. 2006; Robertson & Kravtsov 2007). However, utilizing methodologies such as these becomes computationally infeasible when considering the numbers of simulated galaxies and snapshots modeled in this work.

law with index $\alpha=1.8$ as motivated by observations of local clouds (Blitz et al. 2007), though tests have shown that TURTLEBEACH results do not vary so long as the mass spectrum indices reside within observational constraints (Narayanan et al. 2008b). More details of the implementation of these sub-grid treatments of GMCs may be found in Narayanan et al. (2008a). Within the molecular gas, we conservatively assume that Galactic abundance patterns hold, and model the CO fractional abundance as $\text{CO}/\text{H}_2 = 1.5 \times 10^{-4}$. While molecular abundances in the ISM of high redshift galaxies are unconstrained, recent measurements have shown that star-forming UV-selected galaxies, likely progenitors of massive mergers, have solar abundances in their ISM (Shapley et al. 2004). As such, an assumption of Galactic molecular abundances may be reasonable.

We build the emergent spectrum by integrating the equation of radiative transfer through the H_2 gas:

$$I_\nu = \sum_{r_0}^r S_\nu(r) [1 - e^{-\tau_\nu(r)}] e^{-\tau_\nu(\text{tot})} \quad (3)$$

where I_ν is the frequency-dependent intensity, S_ν is the source function, r is the physical distance along the line of sight, and τ is the optical depth.

The source function is made up of a combination of the emission from dust, as well as line emission. Formally, $S_\nu = j_\nu/\alpha_\nu$ where $j_\nu = j_\nu(\text{dust}) + j_\nu(\text{gas})$. Similarly, α_ν has components from both the gas and dust. The dust radiates as a blackbody, and is assumed to be at the kinetic temperature of the molecular gas. We note that this element of the calculation is inconsistent with the SUNRISE calculations, which formally derives the dust temperature assuming the dust and radiation field are in radiative equilibrium. Here, Weingartner & Draine (2001) opacities are assumed, though this makes little impact on the CO line flux.

The line source function is dependent on the CO level populations. Therefore, in order to self-consistently calculate the line intensities of CO, the molecular excitation properties must be known. The relevant physical processes in determining the CO excitation are collisions and radiative (de)excitation (e.g. line trapping; Narayanan et al. 2008a). The molecules are assumed to be in statistical equilibrium, and the population levels are calculated considering both the radiation field and collisional processes.

The methodology is an iterative one. To determine the solution to the molecular excitation, the level populations across the galaxy are first guessed at (in practice, we guess a solution near LTE). The molecular gas is then allowed to radiate model photons based on the assumed level populations, and, when a sufficient number of photons have been realized in each grid cell, the mean intensity field is calculated (Bernes 1979). Under the assumption of statistical equilibrium, the radiative excitation rates in combination with the collisional excitation rates give updated level populations, and new model photons are then emitted. This process is repeated until the level populations are converged.

The line transfer takes into account velocity fields. The three dimensional velocity field across the model galaxy is returned by the GADGET-3 hydrodynamic simulations. The line of sight velocity gradient from cell to cell is accounted for in the line transfer via emission and absorption line profiles, both of which are Gaussian in nature. The emission and absorption profiles have their widths determined by the thermal line width in the cell, as well as an assumed microturbulent velocity field (here, set at 0.8 km s^{-1}). The difference in the frequency centers of the emission and absorption profiles is determined by the line of sight velocity difference be-

tween the emitting and absorbing clump (e.g. Equations 5 and 6 of Narayanan et al. 2006b).

For the models presented here, ~ 13 million model photons were emitted per iteration. The mass spectrum of GMCs are considered with a lower cutoff of $1 \times 10^4 M_\odot$, and upper limit of $1 \times 10^6 M_\odot$ (consistent with constraints provided by local GMCs; Blitz et al. 2007). The CO excitation was solved for across 10 levels at a time, and the collisional rate coefficients were taken from the *Leiden Atomic and Molecular Database* (Schöier et al. 2005). The boundary conditions included the cosmic microwave background which was modeled at $z=2.2$ to have a temperature of $T=8.74 \text{ K}$.

Finally, we comment that because of spatial resolution limitations in the molecular line radiative transfer, we are forced to consider 8 kpc boxes. Rather than following the center of mass of the merging galaxy system (which, at times, may have scant little gas), we choose to follow a single progenitor galaxy through its evolution. Of course, as the nuclear disks of the progenitor galaxies overlap (both during first passage, as well as coalescence), our models will include the emission from both galaxies in the pair.

2.2.2 Polychromatic SED Radiative Transfer

In order to identify when our simulated galaxies would be selected as submillimeter luminous sources, we simulate the ultraviolet (UV) through submillimeter continuum photometry using the 3D adaptive grid polychromatic Monte Carlo radiative transfer code, SUNRISE (Jonsson 2006; Jonsson et al. 2006, 2009). SUNRISE calculates the transfer of UV through millimeter wave radiation through the dusty interstellar medium. We refer the reader to these work for details on the underlying algorithms as well as numerical tests. Here, we summarize, and explain the physical parameters employed in this study.

The radiative transfer is implemented via a Monte Carlo algorithm in which photon packets representing many real polychromatic photons propagate through the dusty interstellar medium, and undergo scattering, absorption, and reemission. Model cameras are placed around the simulated galaxy to sample a range of viewing angles. The emergent flux is determined by the number of photons that escape the galaxy unhindered in a given camera's direction, as well as those scattered into or reemitted by dust into the camera. For the purposes of the calculations presented here, we used 8 cameras placed isotropically around the model galaxy.

SUNRISE is able to handle arbitrary geometries for the sources and dust. The input spectrum includes contributions from stars and black holes (AGN). The AGN input spectrum utilizes the luminosity-dependent templates of Hopkins et al. (2007) of unobscured quasars. The normalization of the input spectrum is set by the total bolometric luminosity of the central black hole, $L_{\text{AGN}} = \eta \dot{M}_{\text{BH}} c^2$. Again, η is assumed to be 10% (c.f. § 2.1).

The stellar input spectrum is calculated utilizing the stellar populations code, STARBURST99 (Leitherer et al. 1999; Vázquez & Leitherer 2005), where the ages and metallicities of the stars are taken from the hydrodynamic simulations. We assume a Kroupa initial mass function (IMF) (Kroupa 2002), consistent with recent results from observations of $z \sim 2$ star forming galaxies (Davé 2008; Tacconi et al. 2008; van Dokkum 2008). The stellar particles initialized with the simulation are assumed to have formed over a constant star formation history. In order to match the star formation rate and stellar mass of the first snapshot of the simulation, this corresponds to a SFH of $\sim 250 \text{ Myr}$.

The stellar clusters with ages less than 10 Myr are assumed to reside in their nascent birthclouds. SUNRISE models the ef-

fects of reddening of the stellar spectrum through these birthclouds utilizing results from the photoionization code MAPPINGSIII (Groves et al. 2004, 2008). MAPPINGSIII calculates the transfer of continuum radiation and lines through the HII regions (which evolve as a one-dimensional mass-loss bubbles; Castor et al. (1975)) and photodissociation regions (PDRs) surrounding stellar clusters (Groves et al. 2008). The effect of modeling the obscuration of stellar clusters by HII regions and PDRs is a redistribution of emergent UV light into the far infrared/submillimeter bands. The HII regions absorb much of the ionizing UV flux and contribute heavily to the hydrogen line emission from the ISM as well as hot-dust emission. The time-averaged areal covering fraction by PDRs (f_{pdr}) is related to the PDR clearing timescale as $f_{\text{pdr}} = \exp(-t/t_{\text{clear}})$, and is taken to be a free parameter (see Groves et al. 2008). These PDRs absorb much of the non-ionizing UV radiation field, and contribute to the emergent PAH and FIR emission. Here, we assume an areal covering fraction of unity. A covering fraction $f_{\text{pdr}}=1$ translates to a cloud-clearing timescale longer than the lifetimes of O and B stars (Groves et al. 2008), and the main consequence of reducing this clearing time scale is to reduce the emergent submillimeter flux at the time of the starburst (Narayanan et al. 2009). The cloud clearing time scales in gas rich galaxy mergers are unconstrained. That said, some constraints may be placed on this value either by educated guesses, as well as ansatzes that are then verified by a comparison of the simulated SEDs to those observed.

The assumption of a clearing time scale longer than the lifetimes of O and B stars may be a reasonable guess. The centers of local gas rich major mergers are known to have large molecular volume filling fractions, and are well characterized by a uniform, smooth molecular medium (Downes & Solomon 1998; Sakamoto et al. 1999) which may blanket nuclear O and B stars their entire lives. While an assumption of $f_{\text{pdr}}=1$ is not the same as a uniform molecular medium, tests have shown that in this limiting case, the submillimeter SED is the quite similar to $f_{\text{pdr}}=1$ (Narayanan et al. 2009).

Similarly, we can take the reverse approach, and assume the ansatz of $f_{\text{pdr}}=1$, and compare the simulated SEDs to those observed. In Narayanan et al. (2009), we showed that the mean SED in modeled SMGs with a range of masses compares quite well with observed SEDs of SMGs with spectroscopic redshifts. Moreover, those authors found that the peak submillimeter flux was related to the total mass of the galaxy. Utilizing PDR clearing time scales longer than the lifetimes of O and B stars resulted in average ($S_{850} \sim 5$ mJy) SMGs with halo masses of order $\sim 5 \times 10^{12} - 10^{13} M_{\odot}$, consistent with the inferred halo masses of observed SMGs (Swinbank et al. 2008). Similarly, the simulated stellar masses, black hole masses, and H_2 masses both compared well with observations, and scaled with peak submillimeter flux. Reducing t_{clear} (or, equivalently, f_{pdr}) would require more massive galaxies to produce relatively average $S_{850} \sim 5$ mJy galaxies, and quickly violate the inferred halo masses from clustering measurements. As such, the assumption of $f_{\text{pdr}} = 1$ may be reasonable. That said, it is important to interpret the results presented in this paper in the context of this assumption for the birthclouds surrounding stellar clusters, especially in the context of mass-dependent results (such as the CO line widths; § 4.2).

The dust and radiation field are assumed to be in radiative equilibrium, and utilize a method similar to that developed by Juvela (2005). Here, when photons are absorbed in a grid cell, and the dust temperature updated, a new photon with SED equal to the difference between the SED emitted for the new dust tem-

perature and that from the old one is emitted. This procedure is iterated upon until the radiation field has converged (Jonsson et al. 2009). The SUNRISE calculations employ 10 million photon packets per iteration. Jonsson et al. (2009) find that the implementation of dust-temperature iteration in SUNRISE recovers the solution to the Pascucci et al. (2004) radiative transfer benchmarks to within a few percent for UV through mm wavelengths. The Pascucci et al. (2004) benchmarks were recovered through the most stringent test cases of $\tau = 100$. We note that the maximum optical depth we see during the SMG phase of these simulations is $\tau \sim 75$.

The gas and stars initialized with the simulation are assigned a metallicity according to a closed-box model such that $Z = (-y \ln[f_{\text{gas}}])$ where Z is the metallicity, y the yield=0.02, and f_{gas} is the initial gas fraction (though note the fluxes during the SMG phase of the model galaxies are not very sensitive to these assumptions). Because the dust properties of $z \sim 2$ SMGs are relatively unconstrained, we utilize Galactic observations as input parameters. We assume a constant dust to gas ratio comparable to observations of local ULIRGs of 1/50. Tentative evidence suggests comparable dust to gas ratios in SMGs (Solomon & Vanden Bout 2005; Greve et al. 2005; Kovács et al. 2006; Tacconi et al. 2006). Simulations parameterizing the dust in terms of a Galactic dust to metals ratio of 0.4 (Dwek 1998) give similar results to within 10%. The dust grain model used is the R=3.1 Weingartner & Draine (2001) dust model including updates by Draine & Li (2007).

We are exploring the dust and photometric properties of $z \sim 2$ galaxies in a number of companion papers at various stages of preparation. In this work, we focus on the CO properties of SMGs; as such, we primarily utilize SUNRISE as an informant as to when the model galaxies may have sub-mm luminosities comparable to observed SMGs. We classify our model galaxies as SMGs when they have an observer-frame $850\mu\text{m}$ flux ≥ 5 mJy which is comparable to a $3\text{-}\sigma$ detection in current wide-field surveys (e.g. Coppin et al. 2006). We model our sources at $z=2.5$, and therefore this fiducial criterion corresponds to a flux limit at a rest-frame wavelength of $\lambda=243 \mu\text{m}$.

3 EVOLUTION OF SUB-MM, B-BAND AND H_2 PROPERTIES OF SMGS

We begin with a general description of the evolution of the $850 \mu\text{m}$, B -band, and H_2 properties of our model SMGs, and relate these to the evolutionary status of the galaxy merger. In Figure 3, we present the $850 \mu\text{m}$ flux, CO line width (which will be discussed more in § 4.2), and observed B -band apparent magnitude (AB magnitude system, modeled at $z=2.5$, typical of SMGs; Chapman et al. 2003a, 2005) of our fiducial merger simulation, SMG10 (Table 2.1). The blue shaded region represents the sightline dependent range of potential B -band magnitudes. The CO transition plotted is J=3-2 in the rest-frame, corresponding to mm-wave observations at $z \sim 2$. As a reference for the global morphology, in Figure 4, we plot the projected gas density at various snapshots for fiducial model SMG10, with the location of the black holes overlaid.

The initial passage of the galaxies induces a starburst of order $\sim 200 M_{\odot} \text{yr}^{-1}$. The galaxies form stars at this rate for a few $\times 10^8$ yr as they inspiral toward final coalescence. During this time, the galaxy builds a stellar mass of order $\sim 10^{11} M_{\odot}$ (Narayanan et al. 2009). This elevated SFR allows the galaxy to produce $\sim 1\text{-}2$ mJy of flux at $850 \mu\text{m}$ rendering this galaxy below the nominal 5 mJy detection threshold for SMGs, though detectable with future sensitive instruments.

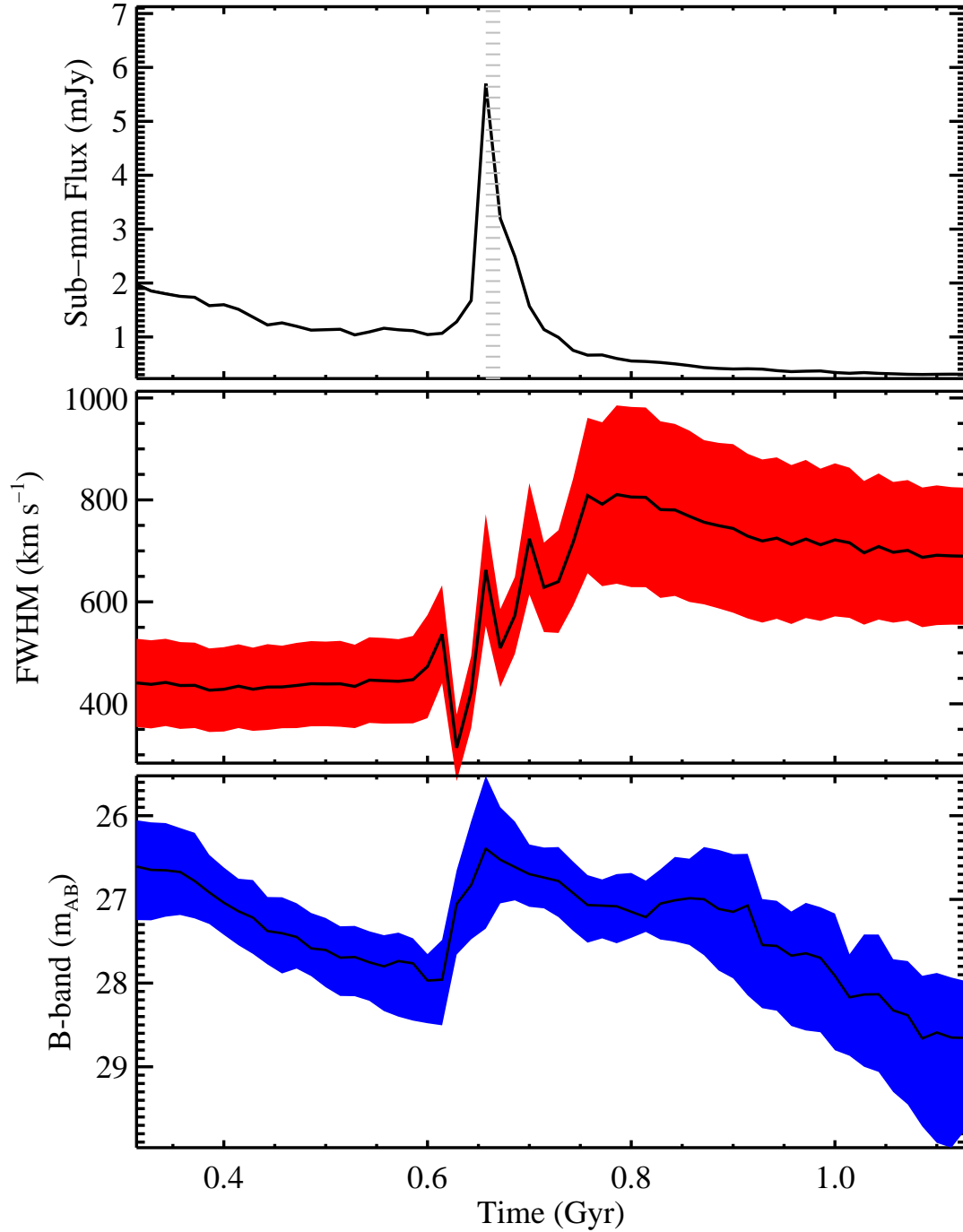


Figure 3. Evolution of 850 μm flux (top row), CO (J=3-2) line width (second row) and observed-frame B -band flux (AB magnitude; third row) for model galaxy SMG10 (Table 2.1, designed to be an average SMG). All quantities are plotted at redshift $z=2.5$. The grey hatched region in the top plot shows when the galaxy is visible as an SMG above $S_{850} > 5$ mJy. The red shaded region in the CO line width plot shows the dispersion over 100 random sightlines, and the blue shaded region in the B -band plot denotes the dispersion over 8 cameras placed isotropically around the galaxy. As the galaxies spiral in toward coalescence, the observed submillimeter flux is relatively low ($S_{850} \approx 1$ mJy), and the progenitor galaxies are disk-like. Consequently, the line widths are representative of the virial velocity of the galaxies (here, set at $V_c = 320$ km s $^{-1}$). As the galaxies coalesce ($T \approx 0.6$ -0.65 Gyr), the $\sim 1000 M_\odot \text{yr}^{-1}$ starburst drives the 850 μm flux to detectable levels ($S_{850} > 5$ mJy). Concomitantly, the B -band flux rises sharply, both owing to the intense starburst and a rapidly growing AGN. The CO line FWHM doubles as two disks enter the simulation box/observational beam (here, set at 8 kpc). In the post-starburst phase, the submillimeter and B -band flux drops, and the line widths settle toward the rotational velocity of the combined (two-galaxy) system. See main text for more details.

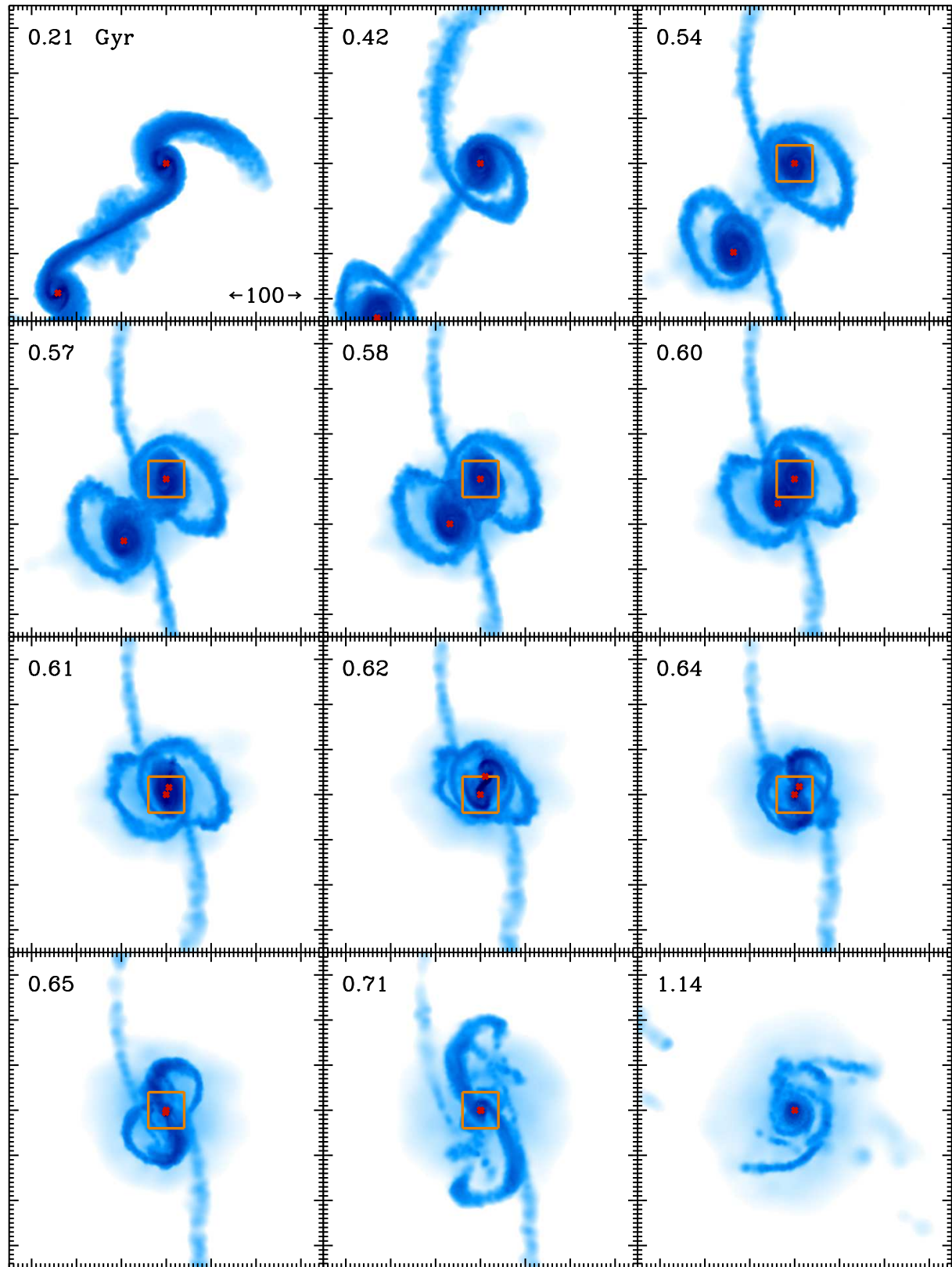


Figure 4. Projected gas density for a fiducial merger model SMG10 (designed to be an average SMG). Box sizes are 100 kpc on a side, and the box centers on the same galaxy the CO calculations center on. The time stamps are in the upper left of each panel, and in units of Gyr. For reference, the SMG phase is at time $T \approx 0.65$ Gyr. Time stamps near the SMG phase have panels with equivalent time stamps to Figures 5 and 7. For these panels, the yellow box highlights the 8 kpc simulation box employed for the CO radiative transfer calculations. The location of black holes is noted by the red crosses.

When the galaxies approach toward final coalescence ($T \approx 0.6$ Gyr), tidal torques from the merger drive large-scale inflows (Barnes & Hernquist 1991, 1996; Mihos & Hernquist 1994, 1996). Physically, the interaction of the galaxies spin up the disks as they transfer angular momentum from the orbit of the galaxies to the disks themselves, and triggers the growth of bars. Gas that shocks on this bar dissipates energy and loses angular momentum, causing an inflow to the central regions (see, e.g. Hopkins et al. 2008, 2009). The high densities in the nuclear region of the coalesced system give rise to a massive starburst of order ~ 1000 - $1300 M_{\odot} \text{yr}^{-1}$. The nascent PDRs surrounding young stellar clusters convert the UV flux intercepted from O and B stars into longer wavelength submillimeter radiation. During this starburst event, the galaxy may be selected as a luminous submillimeter source with $850 \mu\text{m}$ fluxes approaching ~ 5 - 7 mJy (Narayanan et al. 2009). The peak submillimeter flux observed is directly related to the mass of the merging galaxies - galaxy mergers above total (halo) mass $\sim 5 \times 10^{12} M_{\odot}$ will produce the nominal ~ 5 mJy at $850 \mu\text{m}$ to be detectable as an SMG. Mergers of a significantly lower mass will have difficulty producing a strong enough starburst to drive the observed submillimeter flux (Narayanan et al. 2009). This owes to the fact that the submillimeter flux in our model derives largely from reprocessing of UV flux from the starburst in the birth clouds surrounding stellar clusters (Groves et al. 2008).

Concomitant to the final coalescence starburst, inflows fuel central black hole accretion. A fraction of the accreted mass energy is deposited into the ISM surrounding the central black hole(s), driving a pressure-driven wind. These AGN winds expel much of the obscuring gas and dust in the central regions, allowing the system to be viewed as an optically selected quasar ($T \approx 0.65$ - 0.7 Gyr; e.g. Hopkins et al. 2005, 2006; Springel et al. 2005, and references therein). The quasar phase and SMG phase are roughly coincident (though the quasar phase may lag the SMG phase by up to ~ 20 Myr; Springel et al. 2005). This is in good agreement with observations by Coppin et al. (2008b), who find an overlap in a subset of their $z \sim 2$ observed SMGs and quasars. As demonstrated by Figure 3, however, there is a large sightline-dependent dispersion in potential B -band fluxes during the final merger. Consequently, the same galaxy can show almost 2 magnitudes dispersion based on observed viewing angle, and not all SMGs will appear as quasars. However, the galaxy is visible as an SMG at all modeled sightlines.

It is important to note that the selectability of our simulated galaxies as quasars is mass-dependent. As discussed by Narayanan et al. (2009), the final black hole mass of the merged system is dependent on the mass of the galaxy. This is similar to results found by Lidz et al. (2006) and Li et al. (2007) who found that quasar luminosity is tied to progenitor galaxy halo mass. Narayanan et al. (2009) found that the final black hole masses of average SMGs (e.g. $S_{850} \approx 5$ - 7 mJy) will be a few $\times 10^8 M_{\odot}$, whereas the mergers which produce the most luminous SMGs ($S_{850} \approx 15$ - 20 mJy) may make black holes comparable to those seen in quasars ($M_{\text{BH}} \approx 10^9 M_{\odot}$). We therefore continue the discussion of the CO properties of our SMGs during the “quasar phase” as referring to the time period when the simulated dust-attenuated B -band flux peaks (e.g. third panel, Figure 3), and note that this may not necessarily correspond to a galaxy selectable as a quasar in current surveys. The exact relationship between SMGs and quasars will be discussed in due course (J. Younger et al. in prep; D. Narayanan et al. in prep).

The starbursts induced by the merger consume significant amounts of gas. However, while gas consumption is high, supernova pressurization of the ISM sustains large molecular gas

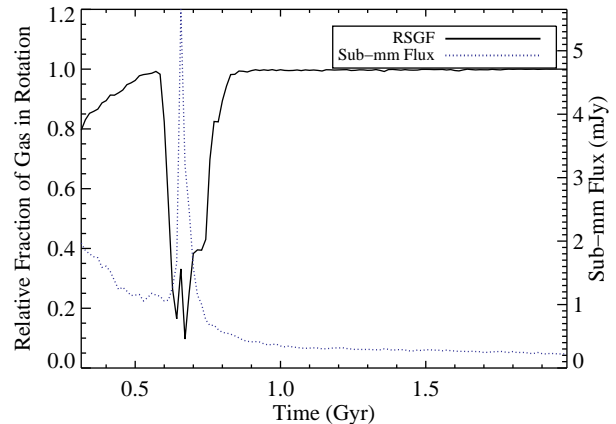


Figure 6. Relative fraction of gas in rotational motion about the galactic nucleus (solid line, units on left axis), and $850 \mu\text{m}$ flux (dotted line, units on right axis) for fiducial merger model SMG10. Following Cox et al. (2009, submitted), gas is considered to be in rotational motion when it has circular velocity at least 75% of the expected Keplerian velocity at its radius. During the peak of the SMG phase, most of the gas is disturbed from the central rotationally supported disk.

fractions. Thermal energy input into the hot phase ISM, as well as mass increases owing to the stellar mass returned and evaporation of cold clouds increases the ambient pressure on cold clouds (Springel & Hernquist 2003). This increase in pressure increases molecular fractions in the neutral ISM, in accordance with our pressure-based H_2 formation/destruction algorithm (c.f. Equation 1). Hence, while star formation of course consumes H_2 gas, during starbursts, this effect may be mitigated owing to conversion of HI to H_2 . The H_2 masses during the final coalescence burst are rather high with typical masses $\sim 5 \times 10^{10} M_{\odot}$, though can be as high as $\sim 3 \times 10^{11} M_{\odot}$ (Narayanan et al. 2009).

4 THE EVOLUTION OF CO PROPERTIES OF SMGS

4.1 CO Morphologies

4.1.1 Molecular Disk Formation and Disruption

The structure of the molecular gas in SMGs, and in particular the (potential) existence of molecular disks is essential to a thorough understanding of the evolution of their CO line properties. We briefly outline the key points related to this topic here, though defer a detailed investigation into the survivability of molecular disks in mergers to a future work.

In Figure 5, we show the CO ($J=3-2$) morphology of galaxy SMG10 as a function of time. The temporal evolution depicts the CO morphology as it evolves through inspiral (first row) and final coalescence (second and third row). The galaxy is most likely to be viewed as an SMG during final coalescence when the SFRs are most elevated (e.g. Figure 1, Narayanan et al. 2009). Here, this corresponds to $T \approx 0.65$ Gyr. Because our CO calculations center around a single galaxy at all points in its evolution to maximize spatial resolution, both galaxies only appear in the images when the nuclei are both within the 8 kpc model box (second row and beyond).

In Figure 6, we show the relative fraction of gas in rotational motion as a function of time, with the sub-mm flux overlaid as a ref-

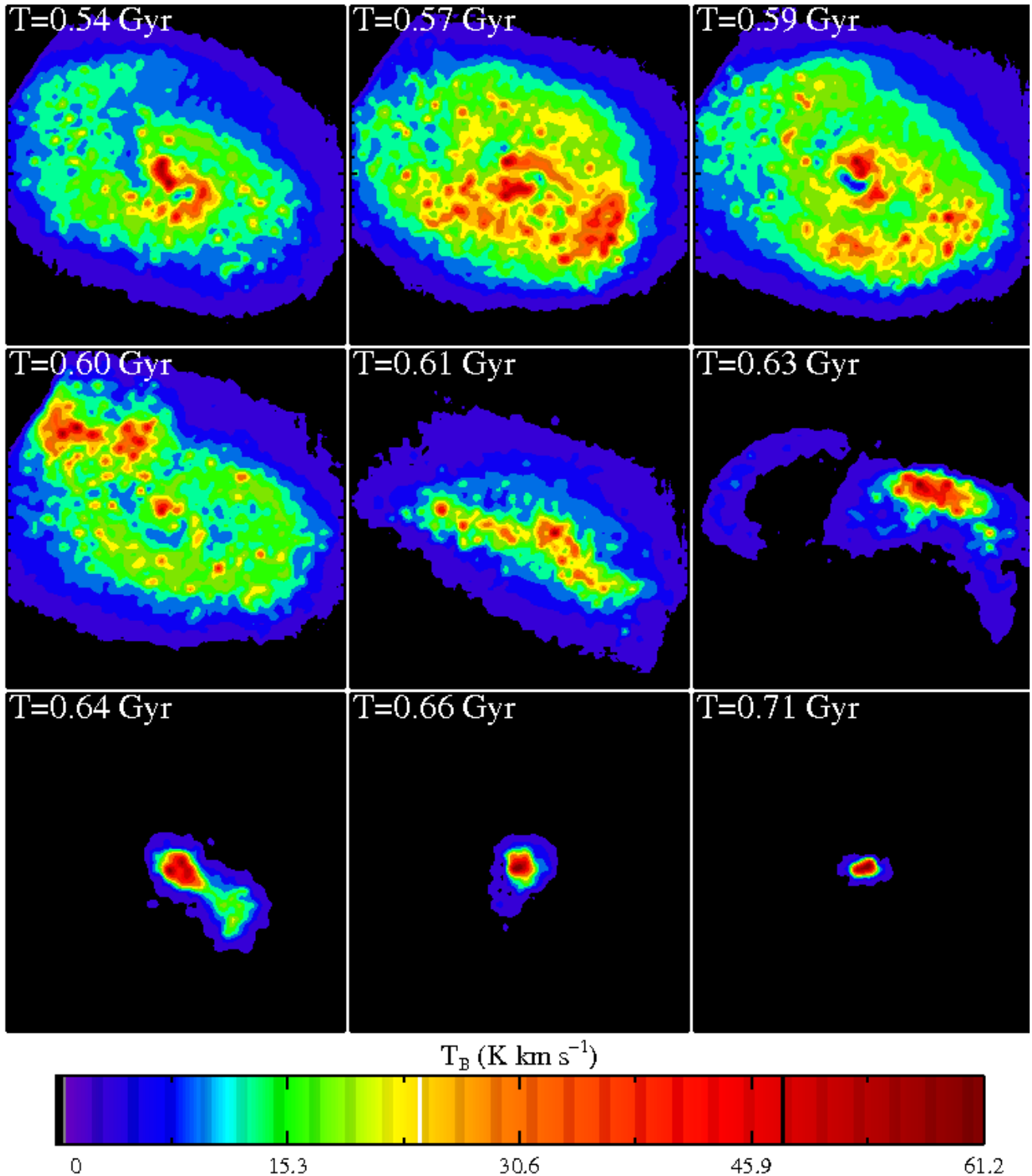


Figure 5. Simulated CO ($J=3-2$) morphology for fiducial model SMG10. The boxes are 8 kpc on a side, and the intensity is in velocity-integrated brightness temperature with scale on bottom. The simulations focus on a single galaxy through its evolution until both galaxies are within a single 8 kpc box (second row and beyond). For reference, the 8 kpc box employed for the CO radiative transfer simulations is shown explicitly with respect to the global morphology in Figure 4. During inspiral (first row of this figure) the molecular gas is in a disk-like configuration. As the second galaxy enters the box, and they merge (second row), the disk-like morphology is disturbed and a large fraction of the gas is pulled from disk-like motion into relatively radial orbits. This corresponds to the peak of the SMG phase. During this time, extended features and tidal tails may become apparent (middle row). Tidal torquing drives much of the gas toward the central regions, resulting in a relatively concentrated molecular gas spatial extent (third row).

erence. Gas is considered to be in rotational motion when its circular velocity exceeds 75% of that expected at its radius for Keplerian motion⁵. As such, the relative fraction of gas in rotational motion may be viewed as a measure of the “diskiness” of the molecular gas. Comparisons between Figures 5 and 6 may be made via the time stamps displayed in the panels of Figure 5.

The galaxies remain relatively disk-like as they inspiral toward final coalescence. Upon final merging, when the galaxy undergoes its luminous SMG phase, the disk is tidally disturbed. Tidal features (and, on occasion, double-nuclei) become apparent in the molecular gas morphology during this final-coalescence SMG phase (e.g. $T \approx 0.65$ Gyr, Figure 5). This can be seen more explicitly in Figure 7, where we plot the CO (J=3-2) centroid velocity maps of the same snapshots shown in Figure 5. Soon after the final interaction/SMG phase, the gas yet again re-virializes, and a strong (compact) molecular disk re-forms (this is seen in Figure 6, though the snapshots in Figure 7 do not extend far enough in time to show this phase). This history of molecular disk formation/disruption throughout the galaxy merger’s history is reminiscent of that seen in models of the molecular ISM in $z \sim 6$ quasars (Narayanan et al. 2008c), and will play an important role in our understanding of the CO line widths, and usage of CO as a dynamical mass indicator in the sections to come.

4.1.2 Spatial Extent of CO Emission

With recent advances in (sub)mm instrumentation, high spatial resolution images of the molecular gas in SMGs is beginning to become available (e.g. Tacconi et al. 2008). Constraints on the spatial extent of the CO emission from SMGs can be important for e.g. determining the dynamical mass from CO line widths.

During the merger-induced starburst, tidal torquing drives cold gas from the outer disk into the nuclear regions of the galaxy. Consequently, the CO emission becomes rather compact. In Figure 8, we plot the distribution of characteristic CO (J=3-2) radii from model galaxies SMG1 and SMG10 over 100 random sightlines during snapshots where the system may be viewed as an SMG ($S_{850} > 5$ mJy). The characteristic radius for CO emission is the flux-weighted standard deviation in the radial distribution of fluxes. Practically, the map is treated as a histogram of fluxes at varying radii. The standard deviation in this histogram is the characteristic radius.

During the SMG phase, the emission is relatively compact owing to the gas funneled into the central regions from the merger. The characteristic radius averages at ~ 1.5 kpc for most sightlines, with some dispersion owing to evolutionary status and sightline. Some large CO radii are seen from inspiralling disks in massive ($M_{DM} \approx 10^{13} M_{\odot}$) mergers which are already SMGs during the inspiral phase (Narayanan et al. 2009).

The CO spatial extents modeled here are comparable to the measurements by Tacconi et al. (2006) of a ~ 4 kpc FWHM diameter in SMGs (which corresponds to a ~ 0.85 kpc standard deviation in radius if the emission is Gaussian in nature). The distribution of radii additionally is consistent with the $\sigma \approx 0.6$ -3.3 kpc range of spatial extents observed from SMGs (Downes & Solomon 2003;

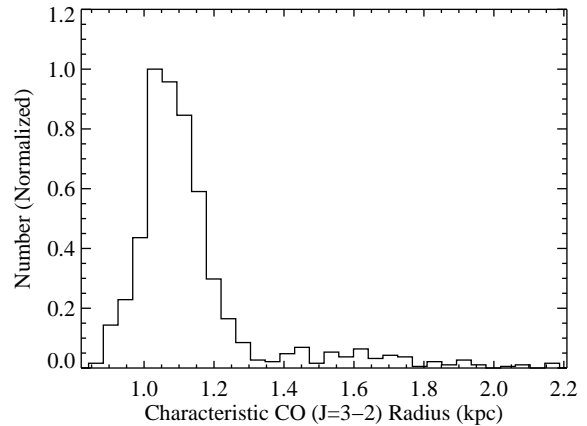


Figure 8. Characteristic radius of CO (J=3-2) emission during the SMG phase of fiducial models SMG1 and SMG10. These models were chosen to bracket the range of masses which produce SMGs (ranging from average, (5-7 mJy), to luminous (~ 15 mJy); Narayanan et al. 2009). The characteristic radius is calculated using the standard deviation in the flux-weighted radial distribution of fluxes. The distribution is plotted over 100 random sightlines. The characteristic radii match up well with observed size scale FWHM measured by Downes & Solomon (2003); Genzel et al. (2003); Tacconi et al. (2006, 2008) and Younger et al. (2008). Please note, however, that because the simulations here are performed in isolation, rather than drawn from cosmological conditions, this distribution represents the range of expected CO (J=3-2) spatial extents from observed SMGs, rather than a true distribution.

Genzel et al. 2003; Tacconi et al. 2006, 2008; Younger et al. 2008; Iono et al. 2009)

4.2 CO Line Widths

4.2.1 Model Results: Evolution of CO Line Widths

The observed molecular line widths of SMGs are exceptionally broad, with a median FWHM of ~ 600 -800 km s^{-1} , and line widths exceeding 1000 km s^{-1} (Greve et al. 2005; Carilli & Wang 2006; Tacconi et al. 2006; Coppin et al. 2008b; Iono et al. 2009). Here, we explore the evolution of CO line widths in our model SMGs; we show how our merger-driven formalism for SMG formation and evolution may self-consistently explain the observed broad lines from SMGs. Because the CO emission line is essentially a distribution measuring the power at a range of molecular gas line of sight velocities, rather than employing any particular fitting methodology (and thus espousing the associated uncertainties), we treat the line as a distribution of fluxes, and utilize the standard deviation of the distribution (σ) as a measure of the line width. For a perfectly Gaussian line, the FWHM of the line would simply be $\sim 2.35 \times \sigma$. While the lines are not perfectly Gaussian, to better compare with observations, we utilize this conversion between σ and FWHM.

In short, the CO line widths are representative of the dynamics of the system (Narayanan et al. 2008c). Prior to final coalescence, typically only a single galaxy is within the beam, and the line widths are narrow, representing the rotational velocity of a single galaxy. During the SMG phase, when the galaxies merge, the line widths roughly double owing to the contribution of emission from both disks. In the post-SMG phase, as the molecular gas relaxes into a new disk (Figure 6), the line widths drop by a factor $\sqrt{2}$.

⁵ Varying this fiducial fraction of 75% makes no difference on the relative temporal evolution of the fraction of disk-like gas; lowering or increasing this value simply increases or lowers the normalization of the curve. As such, throughout this paper, this “fraction” should be taken as relative, and not absolute.

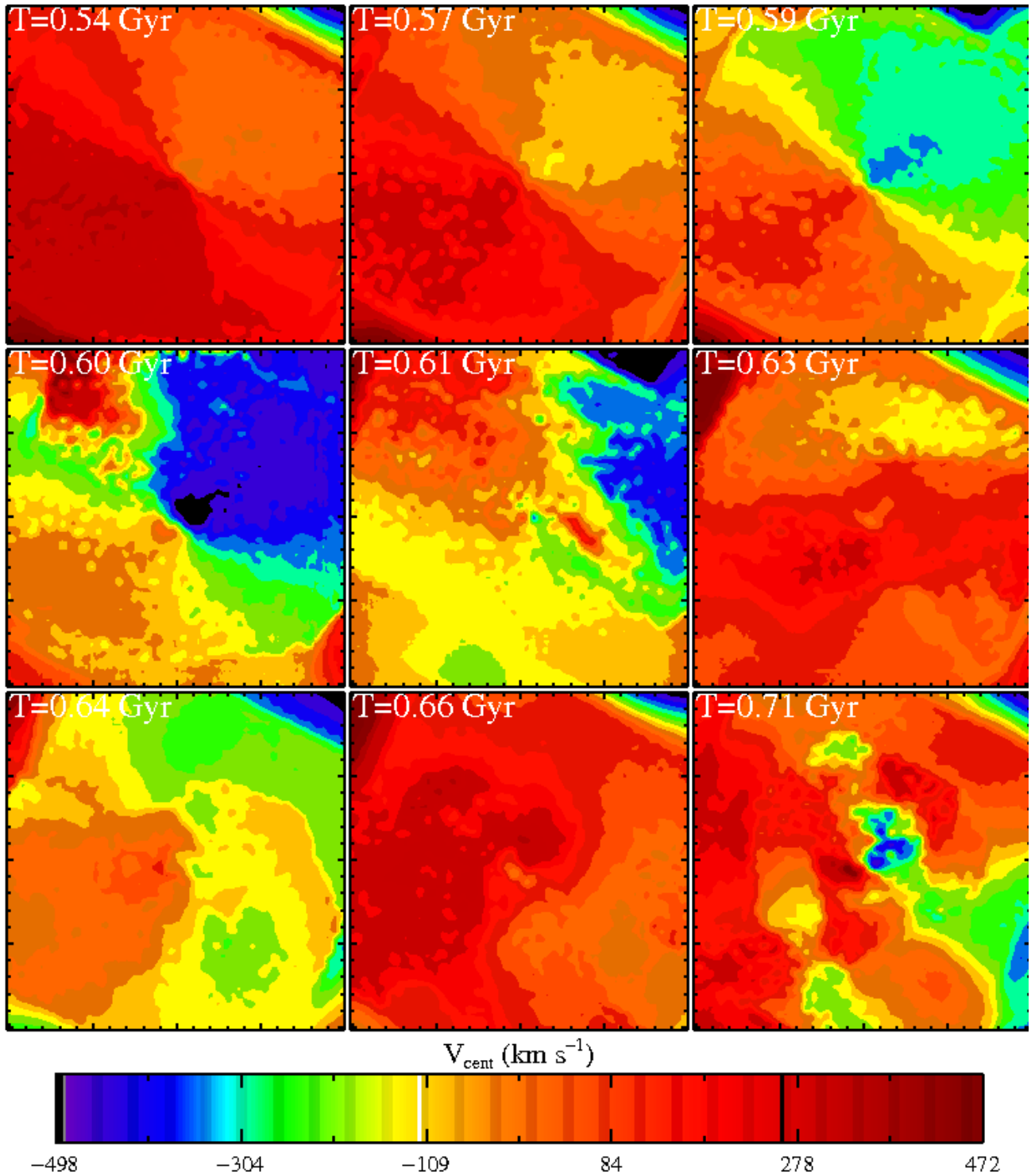


Figure 7. Simulated CO (J=3-2) centroid velocity maps for model SMG10. The boxes are 8 kpc on a side, and the velocity are in units of km s^{-1} with scale on bottom. The snapshots match those of Figure 5. The inspiral phase (top row) is characterized by ordered disk-like motion. The molecular disks are rapidly destroyed as the galaxies coalesce during the SMG phase ($T = 0.63 - 0.65$ Gyr). Note, the disk angle slowly changes throughout the early part of the galaxy's evolution, thus changing the magnitude of the line of sight velocities seen.

In more detail, the CO line widths reflect the dynamics of the molecular gas in the galaxy. This owes to the origin of the CO emission lines from the model galaxy. While emission within a given cell (or neighboring cells) is typically optically thick, globally, the emission is optically thin. When the CO line emitted from a cell escapes the local region, it typically leaves the galaxy unhindered as steep velocity gradients in the throes of the merger shift the absorption profile out of resonance with the emission profile. The CO emission line, then, is essentially the sum of the emission that escapes individual cells containing GMCs at their individual velocities. As such, the line widths are reflective of the dynamics of the system. The dispersion (σ) in the CO line width corresponds well with the velocity dispersion of the gas along the line of sight.

As the galaxies inspiral toward final coalescence, the molecular gas in the progenitor galaxies of the SMG is relatively virialized (Cox et al., 2009, submitted), and thus the line widths are reflective of the circular velocity of the progenitor disks. As discussed in Table 2.1 and Narayanan et al. (2009), our model mergers which produce average SMGs ($S_{850} \approx 5\text{-}7$ mJy) were typically initialized with disks with $V_c = 320$ km s⁻¹, thus resulting in a CO linewidth of $\sigma \approx 160$ km s⁻¹ (which is equivalent to the 320 km s⁻¹ circular velocity in the disk modulated by $\sin(30^\circ)$ to account for the average inclination angle of the disk). This corresponds to a FWHM of ~ 375 km s⁻¹ for a Gaussian velocity dispersion (Figure 3). Recall that during the inspiral phase, typically only one galaxy is within the 8 kpc beam, which is comparable to most interferometric beam sizes (Greve et al. 2005; Tacconi et al. 2006).

When the galaxies coalesce, both galaxies contribute to the detected line. The velocity dispersion of gas detected doubles, and consequently, the line width roughly doubles. This is coincident with the SMG phase. Here, this causes the line widths to increase to $2 \times V_c$. Because the FWHM $\approx 2.35 \times V_c$, and accounting for the average inclination angle of the disks, we then arrive at a generalized expression for the CO line FWHM during the final coalescence SMG phase:

$$\text{FWHM}_{\text{SMG}} \approx 2 \times \sin(i) \times 2.35 \times V_c \quad (4)$$

which is, of course, simply $\text{FWHM} \approx 2.35 \times V_c$ when an average inclination angle of $i=30^\circ$ is assumed. Here, where circular velocities of $V_c=320$ km s⁻¹ are employed for the initialization of the progenitor galaxies, this results in modeled linewidths of $\sim 600\text{-}800$ km s⁻¹. The dispersion in the modeled CO line widths owes to both viewing angle and evolutionary effects.

Generically, the SMG phase and quasar phase occur at or around the nuclear coalescence of the galaxies. However, the exact timing of this event is dependent on a number of things, including galaxy orbit, gas content, and mass, amongst other factors. As such, the CO line widths from the SMGs or quasar host galaxies with a merger-origin show a large range of line widths. In Figure 9, we plot the histogram of CO linewidths from our fiducial galaxy (SMG10) during both its SMG phase as well as its quasar phase. As before, we nominally define the SMG phase as when the 850 μm flux is $\gtrsim 5$ mJy, and arbitrarily define the quasar phase as when the galaxy is brighter than 27th magnitude (AB Magnitude; apparent magnitude at $z=2.5$). Because the SMG phase and quasar phase are nearly coincident, the linewidths are generally broad throughout both phases, with nearly indistinguishable distributions.

4.2.2 Observational Comparisons

The distribution of modeled line widths for SMGs shown in Figure 9 is in excellent agreement with those presented by

Coppin et al. (2008b) and Carilli & Wang (2006). The linewidths are broadly reflective of the mass of the simulated SMGs, and likely signifies a correspondence between the final masses and evolutionary status of our modeled SMGs and those in nature. In this sense, our model faithfully provides a natural explanation for the broad line widths observed in SMGs.

A comparison between the line widths of our model quasars and those in nature is more difficult. Coppin et al. (2008b) presented new CO detections of submillimeter-luminous quasars, and found a nearly indistinguishable distribution of CO line widths from quasars and SMGs, in excellent agreement with the simulations presented here. In both our models, and the observations of Coppin et al. (2008b), the median CO line width is $\sim 600\text{-}800$ km s⁻¹, which we view as a general success of our model. However, a literature compilation of line widths from CO-detected quasars by Carilli & Wang (2006) found a much narrower median in the distribution, with the line widths showing a median value of $\text{FWHM} \approx 300$ km s⁻¹, in contrast to both the observational results of Coppin et al. (2008b) as well as the model results presented here. The source of this discrepancy is not entirely clear. Because the analysis performed by Carilli & Wang (2006) was from a literature compilation, the sample utilized a variety of CO transitions from a non-uniform sample with objects spanning a large range of redshifts from $z \sim 1\text{-}6$. Different CO lines trace different spatial extents, and thus may show a range of line widths. Similarly, quasars even of a similar mass as those presented in Coppin et al. (2008b) but at a lower redshift would naturally show evolution in their line widths owing to shallower gravitational potentials. In contrast, the observations by Coppin et al. utilized only CO (J=2-1) and (J=3-2) emission from a sample of quasars in a smaller redshift range ($z=1.7\text{-}2.6$). In this sense, the comparison between our models and the relatively uniform observations of $z \sim 2$ quasars by Coppin et al. seems most appropriate as it best compares to the redshifts and emission lines investigated in this work.

5 THE USAGE OF CO AS A DYNAMICAL MASS TRACER IN SMGS

In § 4.2, we saw that during the SMG phase of the model galaxy's evolution, the CO line widths were larger than expected from ordered disk-like motion gas. In this context, it is interesting to quantify the usage of CO as a dynamical mass tracer in SMGs.

The exact value of CO line widths in high redshift mergers as a dynamical mass indicator depends, of course, on the relationship between linewidth and dynamical mass assumed. Broadly, for disk-like motion, this relationship can be expressed in the form:

$$M_{\text{dyn}} = k \frac{\Delta V_{\text{fwhm}}^2 R_{\text{hwhm}}}{G \sin^2(i)} \quad (5)$$

where σ is the 1D velocity dispersion in the line, i the disk inclination angle, R the spatial extent of the CO emission (here, taken to be the half-width at half-maximum), and k a constant encompassing the relationship between V_c and V_{fwhm} (for a given distribution of mass) and R_g and R_{hwhm} . Equation 6 holds due to the global optical thinness of molecular line emission across a galaxy.

However, uncertainties exist in all of these conversion factors. Furthermore, it is not clear what fraction of the molecular disk survives during the merger, and whether the inclusion of a $\sin^2(i)$ term is appropriate. Even if it were, prior to the high resolution imaging capable only by ALMA, we can at best assume an average disk

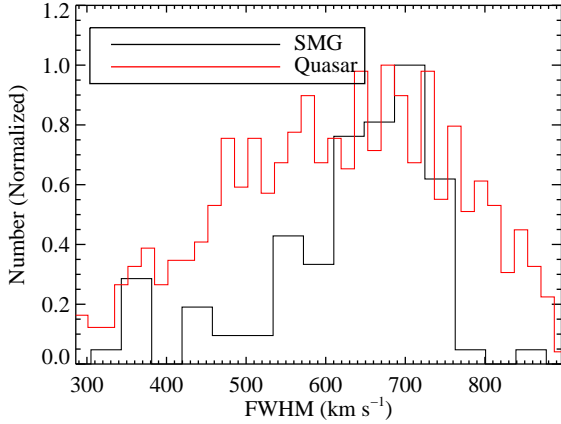


Figure 9. Distribution of modeled CO ($J=3-2$) linewidths during the SMG and “quasar” phases of model SMG10. The SMG phase is considered when $S_{850} > 5$ mJy, and the quasar phase is arbitrarily assigned with an apparent B -band magnitude (AB system) cut of 27th magnitude. See Figure 3 for more details. The phases occur at similar time periods (typically separated by at most ~ 20 Myr), and consequently have similar line width distributions. The FWHM distribution for these two sources appear to correspond well with the distributions published by Coppin et al. (2008b), though the quasar distribution appears to be discrepant with those published by Carilli & Wang (2006). See text for details regarding the origin of the broad CO line widths in SMGs and quasars. Again, because the simulations here are not cosmological in nature, the distribution should be viewed as representative of the range of CO line widths from average SMGs, not the true distribution from a blind survey. While we normally include higher mass models (e.g. SMG1) in our analysis, we refrain here as the extremely broad (FWHM ≈ 1000 - 1400 km s^{-1}) lines from SMG1 take away from the main point of modeled SMGs with average S_{850} fluxes producing average CO line widths. SMGs as massive as SMG1 will be rare (indeed, this is apparent by the relative lack of observed $S_{850} > 15$ mJy SMGs), though when observed, will have line widths FWHM > 1000 km s^{-1} on average.

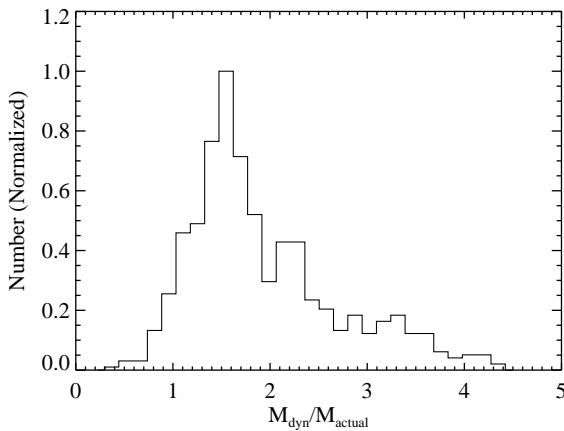


Figure 10. Sightline averaged distribution of $M_{\text{dyn}}/M_{\text{actual}}$ for models SMG1 and SMG10. These models were chosen to bracket the range of masses of galaxies which appear to produce SMGs in our simulations. The dynamical masses are calculated as in Equation 6 for the simulated CO ($J=3-2$) emission. Generally, using CO line widths from SMGs for a dynamical mass calculation requires a modulation of a factor of ~ 1.5 - 2 for translating to a true enclosed mass. See text for details.

angle of $i=30^\circ$. As such, a constructive method for quantifying the usage of CO as a dynamical mass tracer in SMGs is to say:

$$M_{\text{dyn}} = \frac{\Delta V_{\text{fwhm}}^2 R_{\text{hwhm}}}{G} = k' \times M_{\text{actual}} \quad (6)$$

and characterize the relationship between $\Delta V_{\text{fwhm}}^2 R_{\text{hwhm}}/G$ and M_{actual} . Here, note that M_{actual} is the total (baryonic and dark matter) mass enclosed in R_{hwhm} , and ΔV_{fwhm} is calculated as $2.35 \times$ the standard deviation in the line width (c.f. § 4.2). In Figure 10, we plot the ratio of the dynamical mass as calculated in Equation 6 to the true enclosed mass (which includes dark matter and baryonic mass). The radius employed is the half-width at half maximum from the simulated CO emission maps. The ratio of $M_{\text{dyn}}/M_{\text{actual}}$ is calculated for SMGs which span the range of masses explored here, for all snapshots which satisfy the fiducial criteria $S_{850} > 5$ mJy, and for 100 random sightlines. On average, the ratio between the dynamical mass inferred from Equation 6 and the true enclosed mass in the half-mass radius, k' , ranges⁶ from 1.5-1.9. With this, it is then feasible to modulate Equation 6 with this given value of k' to construct the appropriate relationship between CO-derived dynamical mass and true mass enclosed in the CO emitting region.

6 CO EXCITATION AND LINE SPECTRAL ENERGY DISTRIBUTION

The excitation of CO is an important diagnostic of high redshift galaxies. First, molecular line measurements from SMGs are typically made in millimeter bands, which corresponds to high excitation CO lines in the rest frame at $z \sim 2$. Because the inferred molecular gas mass is generally derived via converting CO ($J=1-0$) velocity integrated intensity, understanding the typical CO line ratios (and average level of thermalization of the gas mass within the telescope beam) is crucial. Assumptions of thermalized line ratios (e.g. LTE, when brightness temperature ratios between levels are unity) between higher lying lines and CO ($J=1-0$) may underestimate the molecular gas mass in the event of substantial quantities of subthermal gas. Second, the CO excitation patterns reveal the line(s) of dominant CO power output. As more broadband molecular line spectrometers become available (e.g. the ZEUS, Zspec, Zpctrometer spectrometers; Hailey-Dunsheath et al. (2008); Bradford et al. (2004); Harris et al. (2007)), CO detections of high redshift galaxies will be critically dependent on observations of the brightest lines. In an effort to aid interpretation of existing data sets, and help guide future observations of SMGs, we investigate the molecular excitation properties and CO line ratios from our model SMGs. We do not attempt to address the long standing problem of converting CO ($J=1-0$) flux to H_2 gas mass in galaxies, but rather simply relate the flux density from higher excitation lines to that from the ground rotational transition.

6.1 Model Results: Highly Excited CO in SMGs

In Figure 11, we plot the sightline-averaged model CO SED for models SMG1 and SMG10 (Table 2.1) which bracket the mass range of galaxies that satisfy the nominal selection criteria $S_{850} >$

⁶ Because these simulations are not cosmological, it is not possible to quote an exact mean in the distribution of $M_{\text{dyn}}/M_{\text{actual}}$. This range signifies the range seen when varying the exact model SMG or number of SMGs used to create a distribution similar to that plotted in Figure 10.

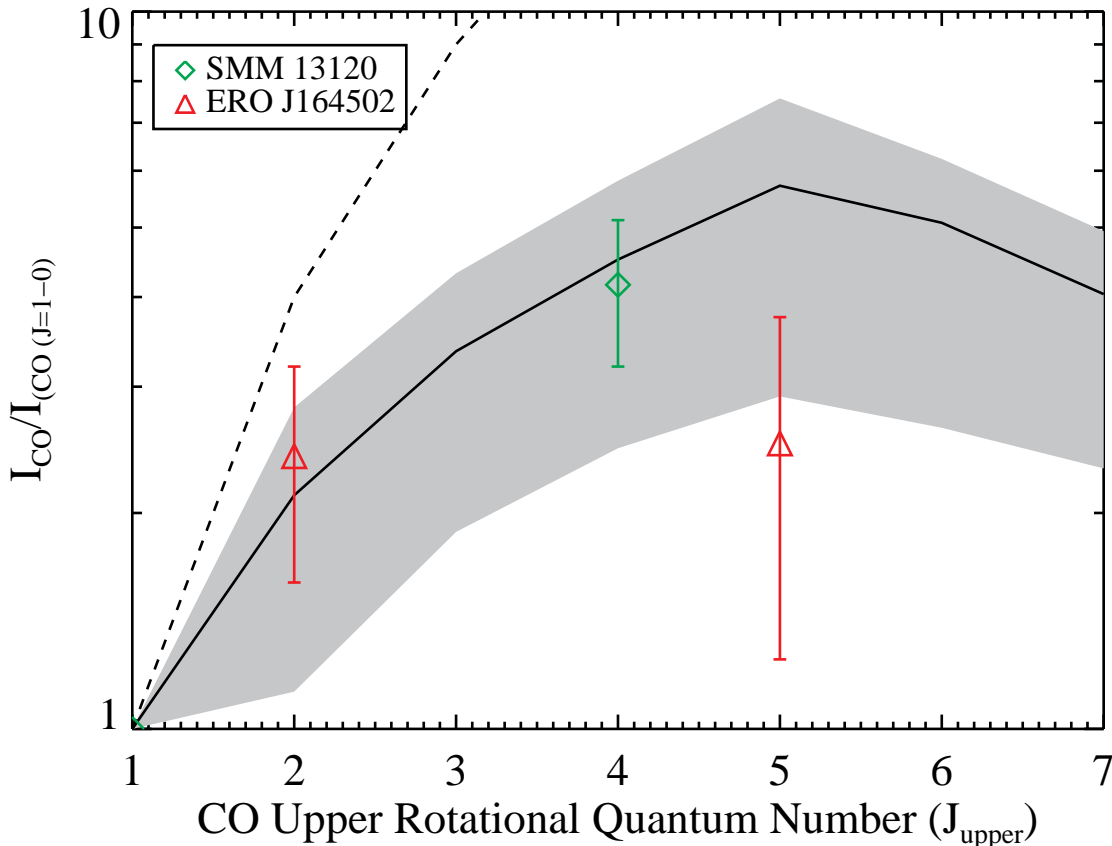


Figure 11. Model CO SED from fiducial models SMG1 and SMG10. The SED is presented for all snapshots where the galaxy would be detected as an SMG ($S_{850} > 5$ mJy), and the solid line shows the mean SED while the grey shaded region denotes the $1\text{-}\sigma$ dispersion amongst snapshots. The flux densities from $J > 1$ levels are compared against the CO ($J=1-0$) level. The dashed line represents the predicted CO SED for thermalized level populations (LTE). The green diamond shows observational data from SMG SMM 13120+4242 (Hainline et al. 2006), and the red triangles from SMG ERO J164502 (aka HR 10) (Andreani et al. 2000; Greve et al. 2003; Papadopoulos & Ivison 2002). To our knowledge, these represent the only SMGs with tabulated multi-line data (including a CO ($J=1-0$) detection) which are unlensed. The highest excitation CO SEDs come from final coalescence mergers, whereas massive SMGs that are above $S_{850} > 5$ mJy during inspiral may have lower CO excitation. The mean SED displays reasonable agreement with the observations, and suggest that CO levels $J \gtrsim 2$ may not be thermalized. This shows that caution must be exercised when assuming a brightness temperature ratio of unity to the CO ($J=1-0$) line when deriving molecular gas masses.

5 mJy. The ordinate is the ratio of the velocity-integrated intensity from various transitions compared to CO ($J=1-0$), normalized to CO ($J=1-0$). The range of emergent CO SEDs from our models is denoted in the grey shaded region, and the mean by the solid line. The dashed line shows the expected CO SED for thermalized level populations. The line ratios are modeled for unresolved observations, and include emission from the entire 8 kpc simulation box. To best compare with the few published constraints (next section), we plot the line ratios relative to the ground ($J=1-0$) transition. This has the added benefit of providing a direct measure of the ability of higher lying transitions to convert to H_2 gas masses.

As Figure 11 shows, there is a broad dispersion in potential CO SEDs from our simulated SMG. However, two generic features are evident. First, on average, the CO is quite excited with the SED turnover only occurring at the $J \approx 5-6$ level. This is in reasonable agreement with observations of $z \sim 2$ SMGs (see next section). The higher excitation CO SEDs come from SMGs which arise during final coalescence mergers, while the lower excitation SEDs represent the inspiral phase of massive galaxies (e.g. SMG1) which

may be seen as SMGs even prior to final coalescence (e.g. Figure 1, Narayanan et al. 2009).

Second, while the turnover is typically at a relatively high J level, most CO levels are subthermal over the 8 kpc simulated box. The rotational ladder in Figure 11 show that the gas is nearly thermalized for the lowest lying lines (CO $J=2-1$). Higher lying lines, however, are not thermalized over the 8 kpc model box. While the gas associated with the nuclear starburst in the central ~ 1 kpc is warm, dense, and thermalized, the outer regions ($R \sim 1-4$ kpc) contain a significant quantity of lower density gas which contributes to the emergent spectrum via line trapping. This lowers the mean excitation conditions observed. As such, Figure 11 demonstrates that most observations of SMGs which do not focus solely on the nucleus will reveal subthermal CO emission at higher-lying ($J \gtrsim 3$) levels⁷. This is effectively saying the filling factor of dense gas is relatively low, thus lowering the mean observed CO SED. *Conse-*

⁷ Higher spatial resolution observations probing the nuclei of SMGs should

quently, assumptions of thermalized CO line ratios from unresolved observations of SMGs will typically underpredict the molecular gas mass.

6.2 Observational Comparisons

While few tabulated observational constraints exist for relative intensities from SMGs, the excitation seen in Figure 11 seems to display reasonable agreement with the existing published data. Line ratios for ERO J164502 and ERO J164502 are given by Andreani et al. (2000); Papadopoulos & Ivison (2002); Greve et al. (2003) and Hainline et al. (2006). These data are represented by the points with error bars in Figure 11. While the CO SED is normalized to the ground state (thus making this point an unconstraining comparison), the higher excitation detection of two lines ($J=2-1$ and $J=4-3$) is entirely consistent with the predictions made here. The intensity from the $J=5-4$ line from ERO J164502 is lower than the models predict here, though we note that this is lowest excitation SMG known (Papadopoulos & Ivison 2002; Weiß et al. 2007).

A detailed survey and compilation of literature data has been presented by Weiß et al. (2007). While these data are not tabulated, we can make qualitative comparisons. The bulk of these galaxies show subthermal emission in the higher lying lines with a turnover at the $J=5$ or 6 level. Thus, at face value, these observed CO SEDs are comparable with the predictions made in Figure 11.

A detailed examination of the Weiß et al. observed CO SEDs, however, suggests a potential discrepancy between the observed values and those modeled here. The observed intensity at the $J=5$ or 6 level (where the SED turns over) is a factor of ~ 15 above that from the ground ($J=1-0$) transition; this is in contrast to our models which suggest that the most excited lines will be only a factor of ~ 5 greater than the ground state (Figure 11). This difference may be reconciled with better constraints on the true CO ($J=1-0$) emission from SMGs. Recall that the CO SED is typically plotted (both here, as well as in observational literature) as relative to the CO ($J=1-0$) transition. For the bulk of the observed sources in the literature, the $J=1-0$ line has not directly observed, but rather inferred from large velocity gradient (LVG) modeling which is simplified approximate method compared to the 3D non-LTE radiative transfer methods employed here. It may be that the apparent difference in excitation between the observations and theoretical predictions will be reconciled via future detections of CO ($J=1-0$) from SMGs.

7 DISCUSSION: TESTABLE PREDICTIONS

7.1 Testable Predictions

In this paper, we have outlined a model for the CO emission from high redshift SMGs. Our models have provided a natural explanation for the observed H_2 gas masses, CO spatial extents, line widths and excitation conditions. We have attempted to compare with literature data when available, and generally found a reasonable correspondence between our model results and galaxies in nature.

This all said, while our models appear to provide a plausible match to observed data, the comparisons made thus far are in essence postdictions. An even more powerful test of any theoretical model would be testable *predictions* of future surveys. In this section, we sketch out potential observable tests of these models which

show higher excitation conditions. This lends itself to a direct testable prediction from these models which we outline in § 7.1.

are imminently possible with the latest generation of bolometer and heterodyne receiver technology.

7.2 CO Linewidths of $z \sim 2$ SMGs and Quasars

Our model for the increased line widths from SMGs relies on a temporary increase in velocity dispersions owing to multiple galaxies in the simulation box/telescope beam. Two features of this model are evident. First, the line widths are relatively low, and representative of the virial velocity of a single progenitor galaxy during the inspiral phase when the observed 850 μm flux may be relatively low ($S_{850} \approx 1$ mJy; Figure 3). They increase concomitant to the increase in submillimeter flux, and are thus broader when the galaxy is in its transient SMG phase, though remain broad in the post-SMG phase when the galaxies 850 μm flux decreases again. In this picture, one might expect a broad range of linewidths from galaxies with lower (~ 1 mJy) 850 μm fluxes: small line widths corresponding to inspiralling galaxies, and large line widths corresponding to post-SMG phase galaxies. Similarly, lower mass mergers (e.g. model SMG13) at final coalescence may contribute to the dispersion of line widths on the low flux end.

Second, as discussed by Narayanan et al. (2009), the 850 μm lightcurve from merging galaxies has a similar shape for a mass sequence of mergers, though scales in normalization. This means that the submillimeter flux curve shown in the top panel of Figure 3 simply scales upward with increasing merger mass (indeed this is evident with a direct comparison of the lightcurve presented in Figure 3 with that of Figure 1 in Narayanan et al. 2009). This means that in more massive mergers, the inspiral phase corresponds to 5 mJy sources, and the peak SMG phase to rarer, more luminous ($S_{850} \gtrsim 10-15$ mJy) SMGs. Consequently, there may be a spread in CO line widths from even 5 mJy SMGs. The most luminous sources, however, only occur at the final coalescence burst of extremely rare $\sim 10^{13} M_{\odot}$ mergers. As such, $S_{850} \approx 10-20$ mJy galaxies will have extremely broad ($\text{FWHM} > 1000 \text{ km s}^{-1}$) CO line widths⁸ with a relatively small dispersion.

The aforementioned effects will have the following generic consequence for CO linewidths from high redshift mergers: the mean CO FWHM will increase with increasing submillimeter flux, and the dispersion will decrease. We show this explicitly in Figure 12 by plotting the sightline-averaged model CO FWHM versus 850 μm flux for model galaxies SMG1, SMG10 and SMG13⁹ in Table 2.1 for a flux limit of $S_{850} > 1$ mJy, and in the middle panel, the CO FWHM-1.1 mm relation. This serves as a prediction for both future sensitive 850 μm surveys, as well as 1.1 mm (e.g. AzTEC; Wilson et al. 2008) counts.

In the right panel of Figure 12, we attempt to compare our model prediction in the left panel with data culled from the recent review by Solomon & Vanden Bout (2005). An important point is that optically selected quasars cannot be included in this sort of comparison as they may preferentially have their molecular disks in a face-on configuration, thus skewing average line widths (e.g. Carilli & Wang 2006; Narayanan et al. 2008c). This does exclude a number of sources which may be simultaneously quasars, and submillimeter bright (e.g. Figure 3 and Coppin et al. 2008b). The

⁸ Recall that the CO line width scales with circular velocity, and consequently, with galaxy mass.

⁹ These models were chosen to span a broad mass range. Note that model SMG13 is too low in mass to form a detectable $S_{850} > 5$ mJy SMG; Narayanan et al. (2009).

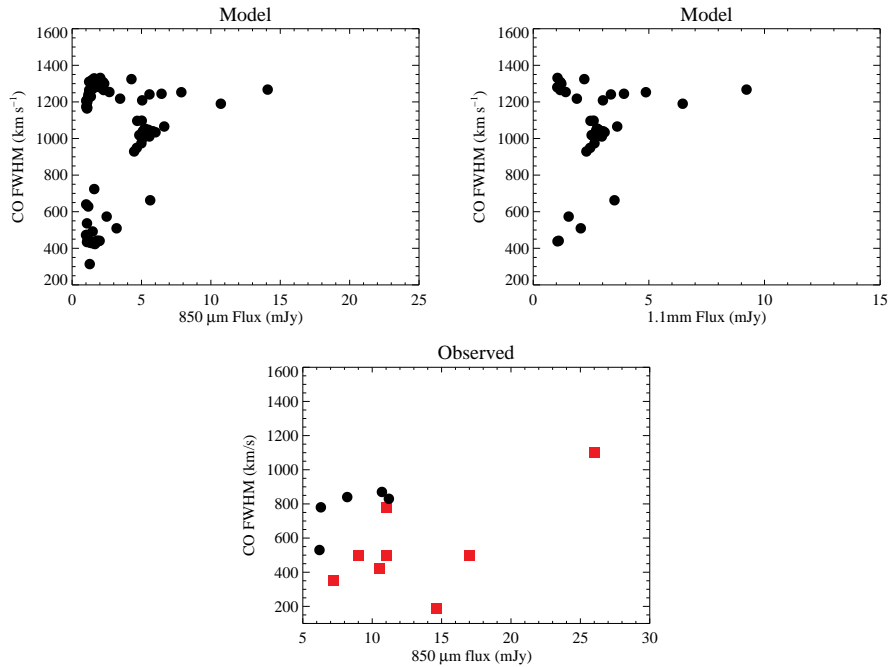


Figure 12. Predicted CO (J=3-2) FWHM- S_{850} relation (left panel), predicted CO (J=3-2) FWHM- $S_{1.1\text{mm}}$ relation (middle panel), and observed FWHM- S_{850} relation culled from data from Solomon & Vanden Bout (2005). The models are for models SMG1, SMG10 and SMG13. SMG1 and SMG10 were chosen as usual to bracket the range of halo masses employed here, and SMG13 added to probe lower fluxes (though note it is too low in mass to ever form a $S_{850} > 5$ mJy SMG). The brightest SMGs at 850 μm and 1.1 mm are predicted to have a narrow dispersion of CO FWHMs, and typically broad lines whereas lower luminosity objects may have a larger range of line widths. The mean CO line width will increase with increasing (sub)mm flux. See text for reasoning. From the observational dataset, optical quasars have been eliminated. The comparison to the observations is generally inconclusive. This may owe to many uncertain gravitational lens magnifications in the observed SMGs (known lensed sources are marked as red squares; Solomon & Vanden Bout 2005). Because these models probe both the full dynamic range of simulated 850 μm fluxes and CO FWHMs, adding more models does not increase the dispersion in the models plots.

observed data in the right panel of Figure 12 are generally inconclusive in comparison to the predictions in the left panel. The effects of uncertain gravitational lens magnifications muddy interpretation (sources that are known to be lensed are marked as red squares; Solomon & Vanden Bout 2005). Better statistics with SCUBA2 and AzTEC will provide a direct and imminent test for this aspect of these models.

7.3 Predicted CO Excitation for High-Resolution Observations of SMGs

With the advent of broadband receivers on a multitude of telescopes, CO SEDs of high redshift objects will soon become available and serve as a test for the excitation predictions outlined in § 6.

We first note that Figure 11 itself is a testable prediction. As few multi-line surveys are currently published, Figure 11 serves as a direct comparative for future constraints on the CO SED from SMGs. A crucial component to this will be the direct detection of CO (J=1-0) emission from SMGs. In the absence of this, relative intensities to this transition will be difficult to interpret, and direct conversion of emission from higher lying transitions to H_2 masses unclear. This is currently feasible at a variety of telescope facilities, though interferometers (e.g. the EVLA) may be preferable as baselines may be problematic on single dish telescopes (Hainline et al. 2006).

Second, we may make predictions for imminent higher spatial resolution observations (e.g. ALMA). The CO excitation con-

ditions presented in Figure 11 for our model SMGs were averaged over the entire 8 kpc box, thus including emission from sub-thermally excited gas. While the gas associated with the nuclear starburst is indeed warm and thermalized, including diffuse, sub-thermal gas had the effect of lowering the mean excitation condition. This is analogous to observations of $z \sim 2$ SMGs which include both dense, nuclear gas, as well as diffuse gas in the telescope beam. Consequently, the modeled excitation conditions in Figure 11 showed excellent agreement with multi-line CO measurements from SMGs.

In principle, one can imagine that higher spatial resolution observations of SMGs which focus on the dense, nuclear regions would show higher excitation CO SEDs. Our approach allows us to quantify this effect, as well as make predictions for the next generation of high spatial resolution interferometers (e.g. ALMA). In Figure 13, we plot the sightline-averaged CO SED for SMG models SMG1 and SMG10 as a function of decreasing physical beam size. As before, we only consider SMGs with a fiducial selection criteria of $S_{850} \gtrsim 5$ mJy. As the observations probe narrower and narrower columns, the observed gas is on average more highly excited, and the turnover point of the CO SED moves to increasingly high rotational number. The lack of complete thermalization in the lower observed transitions (e.g. CO J=2-1) owes to the fact that diffuse gas is still folded into the observation, even for rather high spatial resolution observations.

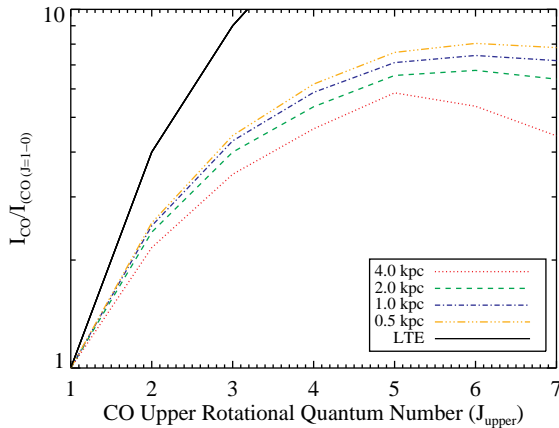


Figure 13. Predicted CO line SEDs for models SMG1 and SMG10 during their SMG phases at increasing spatial resolution. The black solid line shows the predicted CO line SED for thermalized populations. As the warmer, denser gas toward the nucleus is probed, the peak and shape of the excitation ladder shift toward higher levels as more of the gas becomes thermalized. High resolution observations by ALMA of the nucleus of SMGs will typically show higher excitation CO line SEDs than lower resolution observations.

8 SUMMARY

We have combined hydrodynamic simulations of Submillimeter Galaxy formation and evolution with 3D non-LTE molecular line radiative transfer calculations to provide a model for the CO emission properties from SMGs. Our model has shown a number of successes in matching the observed spatial extent of CO emission, CO line widths and excitation conditions. We utilized these models to understand the origin of these emission properties:

- In our model, SMGs originate in major mergers (Narayanan et al. 2009). Strong gaseous inflows drive highly concentrated molecular gas complexes such that the observed characteristic CO radius is of order ~ 1.5 kpc. The large radius tail of the distribution arises from pre-coalescence galaxies in extremely massive ($\sim 10^{13} M_{\odot}$) halos which are SMGs even during the inspiral phase (e.g. Figure 1 of Narayanan et al. 2009).
- The large CO line widths from SMGs owe to the fact that they are typically being observed during a transient phase where the gas is highly non-virialized and multiple galaxies are in the simulation box/telescope beam. During interactions, the CO FWHM from mergers is roughly $2.35\times$ the circular velocity of a progenitor (for a Gaussian line; Equation 4). Two merging $V_c \approx 320 \text{ km s}^{-1}$ disks naturally produce average ($S_{850} \approx 5\text{-}7 \text{ mJy}$) SMGs with extremely broad line widths of order $\sim 600\text{-}800 \text{ km s}^{-1}$.

We have additionally been able to provide interpretation regarding the usage of CO as a diagnostic of physical conditions:

- The usage of CO line widths from SMGs as a dynamical mass estimator may overestimate the enclosed mass. Typical overestimates are of order $M_{\text{dyn}} / M_{\text{actual}} \approx 1.5\text{-}2$.
- The CO excitation in SMGs is high, with the rotational ladder turning over at the $\sim J=5$ or 6 level. The level populations at $J_{\text{upper}} > 2$ are typically subthermal, and assumptions regarding brightness temperature ratios of unity with the ground state will lead to underestimates of the inferred H_2 gas mass. The CO ($J=3\text{-}2$)

line from SMGs is typically a factor of ~ 3 below the intensity expected from thermalized level populations.

Finally, we have made predictions for this model which are imminently testable with the newest generation of bolometer arrays and wide-band sensitive CO receivers:

- The CO line widths from galaxies which will become SMGs are predicted to be their broadest when the submillimeter flux is the highest. Consequently, the brightest SMGs ($S_{850} > 15 \text{ mJy}$) are predicted to only have quite broad (FWHM $> 1000 \text{ km s}^{-1}$) line widths with a small dispersion in FWHMs observed. Lower flux galaxies ($S_{850} \approx 1$) can be either normal disks (where the line widths are predicted to be relatively narrow), or post-SMG phase mergers (where the line widths will be relatively broad). As such, lower flux galaxies are predicted to have a broad dispersion in observed CO FWHM. Care must be taken to both remove optically selected quasars (which may be biased to have face-on molecular disks) and lens-magnified sources from the sample.
- The intensity from the CO $J=5\text{-}4$ or $6\text{-}5$ line, where the CO SED turns over, is predicted to be a factor of $\sim 5\text{-}7$ times that of the ground state. While detections at these higher lying lines are becoming routine, future detections of CO ($J=1\text{-}0$) emission from SMGs will be required to test the predicted rotational ladders.
- The peak and shape of the CO SED will shift toward higher lying transitions as smaller spatial extents are investigated with future high resolution arrays (e.g. ALMA).

ACKNOWLEDGEMENTS

We thank Kristen Coppin, Reinhard Genzel, Thomas Greve, Laura Hainline, and Daisuke Iono for helpful discussions and comments on an earlier draft of this paper. We are extremely grateful to Patrik Jonsson and Brent Groves for their extensive help with SUNRISE. The simulations in this paper were run on the Odyssey cluster supported by the Harvard FAS Research Computing Group. This work was partially funded by a grant from the W.M. Keck Foundation (TJC) and a NSF Graduate Student Research Fellowship (CCH).

References

- Alexander, D. M., Bauer, F. E., Chapman, S. C., Smail, I., Blain, A. W., Brandt, W. N., & Ivison, R. J. 2005a, *ApJ*, 632, 736
 Alexander, D. M., Smail, I., Bauer, F. E., Chapman, S. C., Blain, A. W., Brandt, W. N., & Ivison, R. J. 2005b, *Nature*, 434, 738
 Alexander, D. M. et al. 2008, *AJ*, 135, 1968
 Andreani, P., Cimatti, A., Loinard, L., & Röttgering, H. 2000, *A&A*, 354, L1
 Barger, A. J., Cowie, L. L., Sanders, D. B., Fulton, E., Taniguchi, Y., Sato, Y., Kawara, K., & Okuda, H. 1998, *Nature*, 394, 248
 Barnes, J. E. & Hernquist, L. 1996, *ApJ*, 471, 115
 Barnes, J. E. & Hernquist, L. E. 1991, *ApJ*, 370, L65
 Bernes, C. 1979, *A&A*, 73, 67
 Blain, A. W., Chapman, S. C., Smail, I., & Ivison, R. 2004, *ApJ*, 611, 725
 Blain, A. W., Kneib, J.-P., Ivison, R. J., & Smail, I. 1999, *ApJ*, 512, L87
 Blain, A. W. et al. 2002, *Phys. Rep.*, 369, 111
 Blitz, L., Fukui, Y., Kawamura, A., Leroy, A., Mizuno, N., & Rosolowsky, E. 2007, in *Protostars and Planets V*, ed. B. Reipurth, D. Jewitt, & K. Keil, 81–96

- Blitz, L. & Rosolowsky, E. 2006, *ApJ*, 650, 933
- Bondi, H. 1952, *MNRAS*, 112, 195
- Bondi, H. & Hoyle, F. 1944, *MNRAS*, 104, 273
- Borys, C., Smail, I., Chapman, S. C., Blain, A. W., Alexander, D. M., & Ivison, R. J. 2005, *ApJ*, 635, 853
- Bouché, N. et al. 2007, *ApJ*, 671, 303
- Bradford, C. M., Ade, P. A. R., Aguirre, J. E., Bock, J. J., Dragan, M., Duband, L., Earle, L., Glenn, J., Matsuhara, H., Naylor, B. J., Nguyen, H. T., Yun, M., & Zmuidzinas, J., eds. 2004, Presented at the Society of Photo-Optical Instrumentation Engineers (SPIE) Conference, Vol. 5498, *Z-Spec: a broadband millimeter-wave grating spectrometer: design, construction, and first cryogenic measurements*
- Bullock, J. S., Kolatt, T. S., Sigad, Y., Somerville, R. S., Kravtsov, A. V., Klypin, A. A., Primack, J. R., & Dekel, A. 2001, *MNRAS*, 321, 559
- Carilli, C. L. & Wang, R. 2006, *AJ*, 131, 2763
- Castor, J., McCray, R., & Weaver, R. 1975, *ApJ*, 200, L107
- Chapman, S. C., Blain, A. W., Ivison, R. J., & Smail, I. R. 2003a, *Nature*, 422, 695
- Chapman, S. C., Blain, A. W., Smail, I., & Ivison, R. J. 2005, *ApJ*, 622, 772
- Chapman, S. C., Windhorst, R., Odewahn, S., Yan, H., & Conzelmann, C. 2003b, *ApJ*, 599, 92
- Coppin, K., Halpern, M., Scott, D., Borys, C., Dunlop, J., Dunne, L., Ivison, R., Wagg, J., Aretxaga, I., Battistelli, E., Benson, A., Blain, A., Chapman, S., Clements, D., Dye, S., Farrah, D., Hughes, D., Jenness, T., van Kampen, E., Lacey, C., Mortier, A., Pope, A., Priddey, R., Serjeant, S., Smail, I., Stevens, J., & Vaccari, M. 2008a, *MNRAS*, 384, 1597
- Coppin, K. et al. 2006, *MNRAS*, 372, 1621
- Coppin, K. E. K., Swinbank, A. M., Neri, R., Cox, P., Alexander, D. M., Smail, I., Page, M. J., Stevens, J. A., Knudsen, K. K., Ivison, R. J., Beelen, A., Bertoldi, F., & Omont, A. 2008b, *MNRAS*, 389, 45
- Cox, T. J., Jonsson, P., Primack, J. R., & Somerville, R. S. 2006, *MNRAS*, 373, 1013
- Davé, R. 2008, *MNRAS*, 385, 147
- Davé, R., Hernquist, L., Katz, N., & Weinberg, D. H. 1999, *ApJ*, 511, 521
- Di Matteo, T., Springel, V., & Hernquist, L. 2005, *Nature*, 433, 604
- Downes, D. & Solomon, P. M. 1998, *ApJ*, 507, 615
- . 2003, *ApJ*, 582, 37
- Draine, B. T. & Li, A. 2007, *ApJ*, 657, 810
- Dwek, E. 1998, *ApJ*, 501, 643
- Frayer, D. T., Ivison, R. J., Scoville, N. Z., Evans, A. S., Yun, M. S., Smail, I., Barger, A. J., Blain, A. W., & Kneib, J.-P. 1999, *ApJ*, 514, L13
- Frayer, D. T., Ivison, R. J., Scoville, N. Z., Yun, M., Evans, A. S., Smail, I., Blain, A. W., & Kneib, J.-P. 1998, *ApJ*, 506, L7
- Genzel, R., Baker, A. J., Tacconi, L. J., Lutz, D., Cox, P., Guillelmeau, S., & Omont, A. 2003, *ApJ*, 584, 633
- Greve, T. R., Ivison, R. J., & Papadopoulos, P. P. 2003, *ApJ*, 599, 839
- Greve, T. R. et al. 2005, *MNRAS*, 359, 1165
- Groves, B., Dopita, M. A., Sutherland, R. S., Kewley, L. J., Fischera, J., Leitherer, C., Brandl, B., & van Breugel, W. 2008, *ApJS*, 176, 438
- Groves, B. A., Dopita, M. A., & Sutherland, R. S. 2004, *ApJS*, 153, 9
- Hailey-Dunsheath, S., Nikola, T., Oberst, T., Parshley, S., Stacey, G. J., Farrah, D., Benford, D. J., & Staguhn, J. 2008, in *EAS Publications Series*, Vol. 31, *EAS Publications Series*, ed. C. Kramer, S. Aalto, & R. Simon, 159–162
- Hainline, L. J., Blain, A. W., Greve, T. R., Chapman, S. C., Smail, I., & Ivison, R. J. 2006, *ApJ*, 650, 614
- Harris, A. I., Baker, A. J., Jewell, P. R., Rauch, K. P., Zonak, S. G., O’Neil, K., Shelton, A. L., Norrod, R. D., Ray, J., & Watts, G. 2007, in *Astronomical Society of the Pacific Conference Series*, Vol. 375, *From Z-Machines to ALMA: (Sub)Millimeter Spectroscopy of Galaxies*, ed. A. J. Baker, J. Glenn, A. I. Harris, J. G. Mangum, & M. S. Yun, 82–
- Hernquist, L. 1990, *ApJ*, 356, 359
- Ho, L. C. 2007, *ApJ*, 669, 821
- Hopkins, P. F., Bundy, K., Croton, D., Hernquist, L., Keres, D., Khochfar, S., Stewart, K., Wetzel, A., & Younger, J. D. 2009, *ArXiv e-prints*
- Hopkins, P. F., Hernquist, L., Cox, T. J., Younger, J. D., & Besla, G. 2008, *ApJ*, 688, 757
- Hopkins, P. F., Richards, G. T., & Hernquist, L. 2007, *ApJ*, 654, 731
- Hopkins, P. F. et al. 2005, *ApJ*, 630, 705
- . 2006, *ApJS*, 163, 1
- Hughes, D. H. et al. 1998, *Nature*, 394, 241
- Iono, D., Wilson, C. D., Yun, M. S., Baker, A. J., Petitpas, G. R., Peck, A. B., Krips, M., Cox, T. J., Matsushita, S., Mihos, J. C., & Pihlstrom, Y. 2009, *ApJ*, 695, 1537
- Ivison, R. J., Greve, T. R., Smail, I., Dunlop, J. S., Roche, N. D., Scott, S. E., Page, M. J., Stevens, J. A., Almaini, O., Blain, A. W., Willott, C. J., Fox, M. J., Gilbank, D. G., Serjeant, S., & Hughes, D. H. 2002, *MNRAS*, 337, 1
- Ivison, R. J., Smail, I., Frayer, D. T., Kneib, J.-P., & Blain, A. W. 2001, *ApJ*, 561, L45
- Jonsson, P. 2006, *MNRAS*, 372, 2
- Jonsson, P., Cox, T. J., Primack, J. R., & Somerville, R. S. 2006, *ApJ*, 637, 255
- Jonsson, P., Groves, B., & Cox, T. J. 2009, *ArXiv e-prints*
- Juvela, M. 2005, *A&A*, 440, 531
- Katz, N., Weinberg, D. H., & Hernquist, L. 1996, *ApJS*, 105, 19
- Kennicutt, Jr., R. C. 1998a, *ARA&A*, 36, 189
- . 1998b, *ApJ*, 498, 541
- Kennicutt, Jr., R. C., Calzetti, D., Walter, F., Helou, G., Hollenbach, D. J., Armus, L., Bendo, G., Dale, D. A., Draine, B. T., Engelbracht, C. W., Gordon, K. D., Prescott, M. K. M., Regan, M. W., Thornley, M. D., Bot, C., Brinks, E., de Blok, E., de Mello, D., Meyer, M., Moustakas, J., Murphy, E. J., Sheth, K., & Smith, J. D. T. 2007, *ApJ*, 671, 333
- Keres, D., Yun, M. S., & Young, J. S. 2003, *ApJ*, 582, 659
- Kovács, A. et al. 2006, *ApJ*, 650, 592
- Kroupa, P. 2002, *Science*, 295, 82
- Leitherer, C. et al. 1999, *ApJS*, 123, 3
- Li, Y., Hernquist, L., Robertson, B., Cox, T. J., Hopkins, P. F., Springel, V., Gao, L., Di Matteo, T., Zentner, A. R., Jenkins, A., & Yoshida, N. 2007, *ApJ*, 665, 187
- Lidz, A., Hopkins, P. F., Cox, T. J., Hernquist, L., & Robertson, B. 2006, *ApJ*, 641, 41
- McKee, C. F. & Ostriker, J. P. 1977, *ApJ*, 218, 148
- Menéndez-Delmestre, K., Blain, A. W., Alexander, D. M., Smail, I., Armus, L., Chapman, S. C., Frayer, D. T., Ivison, R. J., & Teplitz, H. I. 2007, *ApJ*, 655, L65
- Mihos, J. C. & Hernquist, L. 1994, *ApJ*, 431, L9
- . 1996, *ApJ*, 464, 641
- Narayanan, D., Cox, T. J., Kelly, B., Davé, R., Hernquist, L., Di

- Matteo, T., Hopkins, P. F., Kulesa, C., Robertson, B., & Walker, C. K. 2008a, *ApJS*, 176, 331
- Narayanan, D., Cox, T. J., Robertson, B., Davé, R., Di Matteo, T., Hernquist, L., Hopkins, P., Kulesa, C., & Walker, C. K. 2006a, *ApJ*, 642, L107
- Narayanan, D., Cox, T. J., Shirley, Y., Davé, R., Hernquist, L., & Walker, C. K. 2008b, *ApJ*, 684, 996
- Narayanan, D., Hayward, C. C., Cox, T. J., Hernquist, L., Jonsson, P., Younger, J. D., & Groves, B. 2009, *ArXiv e-prints: arXiv/0904.0004*
- Narayanan, D., Kulesa, C. A., Boss, A., & Walker, C. K. 2006b, *ApJ*, 647, 1426
- Narayanan, D., Li, Y., Cox, T. J., Hernquist, L., Hopkins, P., Chakrabarti, S., Davé, R., Di Matteo, T., Gao, L., Kulesa, C., Robertson, B., & Walker, C. K. 2008c, *ApJS*, 174, 13
- Neri, R., Genel, R., Ivison, R. J., Bertoldi, F., Blain, A. W., Chapman, S. C., Cox, P., Greve, T. R., Omont, A., & Frayer, D. T. 2003, *ApJ*, 597, L113
- Papadopoulos, P. P. & Ivison, R. J. 2002, *ApJ*, 564, L9
- Pascucci, I., Wolf, S., Steinacker, J., Dullemond, C. P., Henning, T., Niccolini, G., Woitke, P., & Lopez, B. 2004, *A&A*, 417, 793
- Pelupessy, F. I., Papadopoulos, P. P., & van der Werf, P. 2006, *ApJ*, 645, 1024
- Robertson, B., Hernquist, L., Cox, T. J., Di Matteo, T., Hopkins, P. F., Martini, P., & Springel, V. 2006, *ApJ*, 641, 90
- Robertson, B. & Kravtsov, A. 2007, *ArXiv e-prints*, 710
- Robertson, B., Yoshida, N., Springel, V., & Hernquist, L. 2004, *ApJ*, 606, 32
- Sakamoto, K. et al. 1999, *ApJ*, 514, 68
- Schmidt, M. 1959, *ApJ*, 129, 243
- Schöier, F. L., van der Tak, F. F. S., van Dishoeck, E. F., & Black, J. H. 2005, *A&A*, 432, 369
- Shapley, A. E., Erb, D. K., Pettini, M., Steidel, C. C., & Adelberger, K. L. 2004, *ApJ*, 612, 108
- Solomon, P. M. & Barrett, J. W. 1991, in *IAU Symposium, Vol. 146, Dynamics of Galaxies and Their Molecular Cloud Distributions*, ed. F. Combes & F. Casoli, 235–+
- Solomon, P. M. & Vanden Bout, P. A. 2005, *ARA&A*, 43, 677
- Springel, V. 2005, *MNRAS*, 364, 1105
- Springel, V., Di Matteo, T., & Hernquist, L. 2005, *MNRAS*, 361, 776
- Springel, V. & Hernquist, L. 2002, *MNRAS*, 333, 649
- . 2003, *MNRAS*, 339, 289
- Swinbank, A. M. et al. 2004, *ApJ*, 617, 64
- . 2008, *MNRAS*, 391, 420
- Tacconi, L. J. et al. 2006, *ApJ*, 640, 228
- . 2008, *ApJ*, 680, 246
- Valiante, E., Lutz, D., Sturm, E., Genzel, R., Tacconi, L. J., Lehnert, M. D., & Baker, A. J. 2007, *ApJ*, 660, 1060
- van Dokkum, P. G. 2008, *ApJ*, 674, 29
- Vázquez, G. A. & Leitherer, C. 2005, *ApJ*, 621, 695
- Weingartner, J. C. & Draine, B. T. 2001, *ApJ*, 548, 296
- Weiβ, A., Downes, D., Walter, F., & Henkel, C. 2007, in *Astronomical Society of the Pacific Conference Series, Vol. 375, From Z-Machines to ALMA: (Sub)Millimeter Spectroscopy of Galaxies*, ed. A. J. Baker, J. Glenn, A. I. Harris, J. G. Mangum, & M. S. Yun, 25–+
- Weiβ, A., Walter, F., & Scoville, N. Z. 2005, *A&A*, 438, 533
- Wilson, G. W., Austermann, J. E., Perera, T. A., Scott, K. S., Ade, P. A. R., Bock, J. J., Glenn, J., Golwala, S. R., Kim, S., Kang, Y., Lydon, D., Maukopf, P. D., Predmore, C. R., Roberts, C. M., Souccar, K., & Yun, M. S. 2008, *MNRAS*, 386, 807
- Younger, J. D. et al. 2008, *ApJ*, 688, 59